X-ray dark-field contrast imaging of water transport during hydration and drying of early-age cement-based materials

Fei Yang[a,b], Friedrich Prade[c], Michele Griffa[a,*], Rolf Kaufmann[a], Julia Herzen[c], Franz Pfeiffer[c,d], Pietro Lura[a,b]

[a] Empa, Swiss Federal Laboratories for Materials Science and Technology, Überlandstrasse 129, 8600 Dübendorf, Switzerland

[b] Institute for Building Materials (IfB), ETH Zurich, Hönggerberg, 8093 Zürich, Switzerland

[c] Chair of Biomedical Physics, Department of Physics and Munich School of Bioengineering, Technical University Munich, 85748 Garching, Germany

[d] Department of Diagnostic and Interventional Radiology, Klinikum rechts der Isar, Technical University Munich, 81675 München, Germany

Keywords: early-age cement-based materials, water transport, cement hydration, evaporative drying, X-ray dark-field contrast imaging, Talbot-Lau interferometry

ABSTRACT

In this study, we investigated by X-ray dark-field contrast imaging the internal displacements of water in early-age cement-based materials due to their spatial microstructural heterogeneities. We performed time-lapse multi-contrast X-ray radiography measurements with a laboratory-scale Talbot-Lau X-ray interferometer during drying and hardening of a model system. Such system consisted of two mortar layers with distinct pore size distribution and local porosities. With these measurements we propose a new approach to imaging water transport in such materials at early hardening ages.

The results show that such approach provides higher sensitivity to local water content changes and higher temporal and spatial resolutions as compared to standard X-ray attenuation contrast imaging. In this work, we assessed both qualitatively and quantitatively the roles of key drivers of such water displacements in the evolving microstructure: capillary force gradients created by the spatial heterogeneity in the pore size distribution and by evaporative drying. This was accomplished by correlating the dark-field contrast imaging results with information about the system's pore space features, obtained by attenuation contrast X-ray microtomography and respective 3D image analysis. Such correlative analysis provides new evidence of the existence of strong couplings between pore-scale water displacements and the microstructure formation in cement-based materials at early ages.

*Corresponding author at: Empa, Swiss Federal Laboratories for Materials Science and Technology, Switzerland. Tel: +41 58 765 4360. Email address: michele.griffa@empa.ch

Keywords: early-age cement-based materials, water transport, cement hydration, evaporative drying, X-ray dark-field contrast imaging, Talbot-Lau interferometry

ABSTRACT

In this study, we investigated by X-ray dark-field contrast imaging the internal displacements of water in early-age cement-based materials due to their spatial microstructural heterogeneities. We performed time-lapse multi-contrast X-ray radiography measurements with a laboratory-scale Talbot-Lau X-ray interferometer during drying and hardening of a model system. Such system consisted of two mortar layers with distinct pore size distribution and local porosities. With these measurements we propose a new approach to imaging water transport in such materials at early hardening ages.

The results show that such approach provides higher sensitivity to local water content changes and higher temporal and spatial resolutions as compared to standard X-ray attenuation contrast imaging. In this work, we assessed both qualitatively and quantitatively the roles of key drivers of such water displacements in the evolving microstructure: capillary force gradients created by the spatial heterogeneity in the pore size distribution and by evaporative drying. This was accomplished by correlating the dark-field contrast imaging results with information about the system's pore space features, obtained by attenuation contrast X-ray microtomography and respective 3D image analysis. Such correlative analysis provides new evidence of the existence of strong couplings between pore-scale water displacements and the microstructure formation in cement-based materials at early ages.

1. Introduction

Water transport occurs inside cement-based materials at early ages immediately since casting time. That is because of a highly heterogeneous spatial distribution of capillary forces inside the pore space. On one side, such heterogeneous distribution is caused by (1) the spatial heterogeneity and temporal evolution of the pore size distribution and (2) by evaporative drying [1,2]. On the other side, such transport significantly influences the microstructure evolution, thus the macroscopic poro-mechanical and fluid transport properties of the hardened materials. The influencing is not uni-directional. Rather, couplings and feedback loops exist between how the microstructure evolves and how consequently water moves through the evolving pore space [3].

The availability of methods for imaging early age water transport has a significant practical impact on developing approaches for improving the long-term durability properties of cement-based materials. Examples of such approaches include the mitigation of early-age shrinkage processes, e.g., plastic [4] and drying shrinkage [5]. Another important example is the achievement by internal curing [6–8] of higher degrees of hydration in low water-to-cement ratio (w/c), i.e., high and ultra-high performance, concretes. A final example is related with the optimal design of repair materials [9,10].

Evaporative drying leads to the formation of water menisci inside the pore space, typically starting from the surface(s) exposed to the environment, then progressing inside the bulk of the specimen. The heterogeneous spatial-temporal distribution of such menisci leads in turn to the development of very heterogeneous capillary force field gradients, responsible, at different

early-age stages, of plastic shrinkage and drying shrinkage, respectively. Understanding the couplings between the microstructure formation, including the shrinkage-induced microcracks, and the evaporative drying progression inside the specimen is functional to the development of shrinkage reduction approaches based, e.g., upon shrinkage reducing admixtures [4] or internal curing water-saturated particles [8].

Internal curing particles, e.g., light weight aggregates (LWAs) or super absorbent polymers (SAPs), have been used as internal reservoirs and suppliers of water. They are saturated before or directly during the mixing and uniformly dispersed in the cast volume, thus providing a spatially homogeneous supply of curing water [8]. Such supply to the hydrating cement matrix is thought of being driven by local capillary force gradients, which are dependent upon the local microstructure formation [11]. The optimization of internal curing methods requires a complete understanding of how and how far is water displaced from the more porous LWAs or from the SAP particles to the less porous cement matrix [12].

Cement-based composites for repair of already hardened concrete structures also rely upon an accurate understanding of how water is displaced by capillary force gradients generated by the spatial heterogeneities in the pore system. As hypothesized by Bentz et al., when the repair layer is designed to achieve a pore size distribution with a prevalence of the larger pores, compared with the substrate, the adhesion between the repair layer and the substrate could be increased by water capillary suction towards the substrate [1,2].

In their work, Bentz et al. were among the first to use model systems for investigating the role played by capillary force gradients in water transport at early ages. They did so by spatially mapping the temporal evolution of a proxy variable of local water content. The model systems they used consisted of different combinations of two layers of distinct cement pastes, one cast on top of the other in sealed or open molds. The cement pastes differed either in w/c value [1,2] or in cement particle size distribution [1]. In either case the overall effect was that of creating different pore size distributions for the two distinct layers. Independently of the position of the two distinct pastes, either at the bottom or at the top of the mold, and independently of sealing the top or not, a relative increase in local water content was observed for the layer with finer pores. On the contrary, a relative decrease was observed for the layer with coarser ones.

These results provided the first systematic evidence, for cement-based materials, of the movement of water from the “coarser pores layer” to the “finer pores” one. Even in the case of an open mold and the layer with finer pores on top of the other one, thus exposed to a lower relative humidity (RH) environment and subjected to evaporative drying, the bottom layer, not directly exposed to the lower RH, was observed to lose water. Moreover, the bottom layer started losing water earlier than the top one. This likely occurred by water displacements from the larger pores of the bottom layer to the smaller ones in the above layer. This observed loss in the “sealed” bottom layer suggests that water can be displaced not only by capillary force gradients created by evaporative drying, as it is well known from the poro-mechanics of dry-

ing [13,14], but also by capillary force gradients produced by intrinsic spatial gradients in pore size range and pore size distribution.

The experiments of Bentz et al. [1,2] were among the first results with broad impact on the understanding of water movement at early ages during the simultaneous and coupled microstructure formation and evaporative drying.

One consequence of such experimental observations was the description of drying mechanisms in computational models of hydrating cement-based materials [1]. In addition, these were the first measurements consisting of imaging, by X-ray attenuation measurements, the spatial-temporal distribution of water at early ages, even though only 1D spatial profiles could be obtained.

Since those first studies [1,2], the visualization of water transport in early age cement-based materials has been achieved by different imaging techniques.

Three of the most commonly used techniques have been neutron imaging (NI), magnetic resonance imaging (MRI) and X-ray attenuation-contrast imaging (XACI).

NI has been widely used for both visualizing and quantitatively characterizing a large variety of water transport processes in cement-based materials [15]. This is because of the large total interaction cross section of a neutron with hydrogen, leading to high contrast to spatial differences in local water content and to their changes.

Examples of NI applications, related with water displacements at early ages, include visualizing the release of internal curing water provided by saturated LWAs and the water movement across the surrounding cement [16,17] or mortar matrix [18]. Another example is related with the visualization of the release and movement of internal curing water provided by saturated SAP particles [19,20]. The last example regards locating the redistribution of water in fresh mortars exposed to external drying, leading to their plastic shrinkage and cracking [21].

Despite these applications (along with many others) to hardening cement-based materials show the usefulness and potential of NI, this technique has two main limitations. The first one is its limited accessibility, due to the small number of neutron facilities world-wide and to the time constraints in using them. The second main limitation is the maximum spatial and temporal resolutions, currently not sufficient for pore-scale investigations. The spatial resolution does not exceed yet the length scale of 10-20 μm at state-of-the-art facilities [22], even though current developments may reduce these limits to the scale of a few μm [23,24]. The maximal temporal resolution does not allow yet investigating in 3D such fast displacements driven by large capillary force gradients, e.g., the capillary suction of water from a more porous region or from a porous internal curing particle to a less porous one [17,21].

MRI has the advantage of allowing mapping quantitatively the local water content and, simultaneously, the local pore size distribution, the latter by nuclear magnetic resonance relaxometry, all feasible at the laboratory-scale [25,26]. In addition, different types of in-pore water can be distinguished and spatially mapped, still by NMR relaxometry. Thus, the two types of

mapping have been successfully used for the investigation of the couplings between the microstructure evolution and the water displacements induced by evaporative drying [27]. However, compared to neutron imaging, this technique achieves even lower spatial and temporal resolutions [28]. Also the high cost of a scanning MRI instrument makes it less affordable by any laboratory.

X-ray attenuation contrast imaging (XACI) has so far achieved both high spatial (down to a few hundreds of nm) and high temporal (down to a few hundreds of ms, for tomography) resolutions in studying, in general, water transport in porous materials. Such achievements have been obtained not only at synchrotron radiation facilities [29,30] but also with more accessible and widespread laboratory-scale setups [31], whose availability is typically higher than MRI instruments', due to much lower costs.

XACI is based on measuring the attenuation of an X-ray beam transmitted through the specimen. The pixel value in single 2D projection images (radiographs) reflects the accumulated projection of the specimen's attenuation coefficient μ along the ray traced from the X-ray source to the detector's pixel (Beer-Lambert law). μ is related to the imaginary part, β, of the complex index of refraction n of the specimen,

$$n = 1 - \delta + i\beta, \quad (1)$$

where δ is the real part of such index (decrement thereof, respect to the unity) and i is the imaginary unit.

β is linearly proportional to n_e, to $Z^n$and to E^{-m}. n_e is the electron density, Z is the atomic number of a predominant composing element, with $n \cong 4 - 5$, and E is the photon energy, with $m \cong 3 - 3.5$ [32]. The contrast to local changes in water content strongly depends on the relative differences between water, air and the solid substrate, in terms of n_e and/or Z. For the majority of porous building materials, such differences are typically very small, leading to low contrast to local water content changes. Despite the low contrast, previous studies have shown that XACI can still allow visualizing water transport in porous materials when either the pore size ranges from hundreds of μm to tens of mm [33] and/or the water content change involves large volumes of water relatively to, e.g., the voxel size of the X-ray tomogram [34]. The last condition may be for example achieved when only 2D radiographs are acquired, each pixel value being the sum of μ values along the corresponding ray intercepting the specimen volume along the beam direction (thickness, T). Most of the studies published so far and dealing with XACI of water transport in cement-based materials at early age have exploited the latter condition, which is not always fulfilled and depends upon the saturation degree and T, or they have exploited rather low X-ray energies (30-40 keV) at which most of the laboratory X-ray imaging setups do not operate [1,2,12,35–38]. Thus laboratory scale XACI is also affected by strong limitations in studying water transport in early age cement-based materials.

The limited contrast to local water content changes has been so far overcome in most of the studies by substituting pure water with water-based salt solutions, the salt being used as a con-

trast agent. Examples of contrast agents used with cement-based materials are lead nitrate [39] and cesium carbonate [40], used to investigate liquid transport through cracks in concrete. Other examples of contrast agents frequently used with other porous building and geo-materials are calcium iodide (CaI), used to study evaporative drying in experimental models of soils [41], and cesium chloride (CsCl) [29,42–44] or potassium iodide (KI) [45–47], used for imaging pore-scale multi-phase fluid displacements and respective interfacial mechanisms.

Despite its widespread use for XACI of liquid transport in porous materials, the application of contrast agents to investigating early-age water transport in cement-based materials remains unfeasible, due to their interference with cement hydration, thus with the microstructure formation and evolution.

Two complementary X-ray imaging methods, developed in the last two decades and available also with laboratory scale sources, have been recently shown sharing the advantages of XACI, in terms of spatial resolution, and providing a possible solution to the problem of low contrast to local water content changes, also for early-age cement-based materials, without the need of using contrast agents.

The first method is called X-ray phase-contrast imaging (XPCI). It consists of producing radiographic or tomographic images whose pixel/voxel values are based upon the linear projection or the direct values of δ (see Eq. (1)). In previous work, we have demonstrated, for porous building materials, the higher sensitivity of XPCI to pure water content changes in pores with size above the spatial resolution of the tomograms, compared with corresponding results obtained, on the same specimens and with the same X-ray source and detector, by XACI [48,49]. The reason for the higher contrast by XPCI is twofold: 1) the difference in δ values between pure water and air, normalized by the δ value of the solid substrate, is larger than the respective normalized difference for the β values (see Figures 4(a) and (b) in [49]); 2) δ achieves larger values than β, for both water and any material phase of the solid substrate, e.g., cement hydration products (see Figure 4(c) in [49]), and at any X-ray photon energy.

The first fact implies that pore-scale water displacements can produce a larger pixel/voxel value change when the pixel/voxel value itself is related with the local δ value than the β one: any water gain to or loss from a pixel/voxel, containing both the solid phase and a pore, will have smaller impact to the change in the pixel/voxel value if it is based upon β than upon δ.

The second fact implies that, specifically for pores with size above the spatial resolution of the images, a partial or complete filling/emptying by water is more likely to produce local changes in the image when it is based upon δ than β.

Several XPCI implementations mainly or only exploit synchrotron radiation sources, because they require an X-ray beam with high spatial coherence. That is the case for XPCI based upon a crystal analyzer [50] and free space propagation [51,52]. However, in the last decade new approaches have been pursued for performing XPCI using also laboratory sources, namely

edge illumination (EI) [53], speckle pattern analysis (SPA) [54,55] and X-ray Talbot-Lau interferometry (TLI) [56,57]. The latter techniques bear an additional advantage: they allow obtaining, from the same measurement session, both the linear projection of β and of δ plus the linear projection of the 3D spatial distribution of a variable here called ϵ and phenomenologically defined as an (ultra-)small angle X-ray scattering, (U-)SAXS) "strength", as introduced in [58] for TLI. From sets of linear projections, the actual 3D spatial distribution of each of the three variables can be retrieved by tomographic reconstruction [58]. Thus, three tomograms can be obtained from a single measurement, with complementary information.

Producing images based upon ϵ is typically termed X-ray dark-field contrast imaging (XDFCI). The contrast in such images stems from the heterogeneity in the spatial distribution of δ at a length scale below the spatial resolution of the imaging system, which we call sub-resolution heterogeneity. Such heterogeneity contributes to create (U-)SAXS. The overall, macroscopic-scale consequence of the (U-)SAXS occurrence is a reduction in amplitude and a further distortion of the periodic (Talbot) interference pattern. The spatial mapping of such reduction and distortion allows for a qualitative mapping of the degree of sub-resolution heterogeneity.

Even though (U-)SAXS as a physical process is considered to play a key role in forming the X-ray dark field contrast, XDFCI does not provide directly the same data as obtained in a traditional (U-)SAXS measurement. In the latter, a monochromatic pencil beam is typically used for illuminating the specimen at a specific point. The correspondingly transmitted beam is measured in the Fraunhofer diffraction range of the specimen at the used photon energy. Such spatial distribution of the beam at that range is the (U-)SAXS pattern. It is directly related with the spatial Fourier transform of the auto-correlation function, $G(r)$, of the sub-resolution heterogeneity (see Eq. 3'' in [59] and Eq. 4 in [60]). The features of such function embed quantitative information about the sub-resolution heterogeneity at the illumination point. For example, the auto-correlation length, r_{auto}, is defined as the distance between two points at which the auto-correlation function achieves a global minimum. Such length is related to a characteristic length scale of the sub-resolution heterogeneity. For example, in the case of a statistically homogeneous and isotropic dispersion of overlapping spherical "particles" with diameter D, it has been shown that $r_{auto} \cong D$ (see Section 5.1.1 of [61]). "Particle" is here intended with the common meaning of a heterogeneous inclusion in a homogeneous matrix (see Chapter 2 of [61]), e.g., a pore in a continuous, solid material phase.

Such type of information, in the case of XDFCI, is embedded in the local modifications of the Talbot interference pattern by the specimen's scattering, quantified by the variable ϵ. This occurs even though during a TLI measurement no traditional (U-)SAXS pattern is actually acquired in the Fraunhofer diffraction region of the specimen.

Several theoretical studies have demonstrated that the phenomenological variable ϵ is directly proportional to the product of the macroscopic scattering cross-section, Σ, and of the auto-

correlation function of the sub-resolution heterogeneity, $G(\zeta_{interf})$, sampled at a specific correlation distance ζ_{interf} which depends only upon the interferometer configuration, under the assumption of elastic scattering [62–64]. These theoretical results are based on a few assumptions, the most important of which are the presence of a periodic intensity interference pattern illuminating the specimen and scattering at small angles by the specimen's sub-resolution heterogeneity. The theoretical framework describing such X-ray dark-field contrast has been accompanied by experimental validations for model systems, e.g., colloidal suspensions [63,64]. For such systems, analytical formulations of $G(r)$ are available and they have been experimentally validated by corresponding (U-)SAXS measurements.

A key important result of such theoretical framework is the relationship between ϵ and $G(\zeta_{interf})$. The latter suggests that by performing multiple XDFCI measurements, with distinct configurations, thus distinct ζ_{interf} values, it is possible to retrieve $G(r)$, thus to quantify descriptors of the sub-resolution heterogeneity which have been typically obtained with standard (U-)SAXS measurements. The advantage of XDFCI resides in its full-field nature, i.e., the possibility of obtaining by full illumination of the specimen volume a spatial distribution of (U-)SAXS-like descriptors which would otherwise need a point-by-point determination by standard scanning (U-)SAXS measurements. However, the spatial scanning is substituted by an "instrument-configuration" scanning, i.e., a scanning of a range of possible ζ_{interf} values.

In the study presented in this article, no quantitative retrieval of $G(r)$ or of Σ was pursued and compared with similar quantification from standard (U-)SAXS measurements. Rather, we aimed at spatially mapping the linear projection of ϵ by XDFCI in radiographic mode for mapping sub-resolution heterogeneity changes with time due to the coupled local water content changes and the actual microstructural changes.

Indeed, as shown in our previous work by TLI, in addition to microstructural changes, the saturation/desaturation of pores by pure water in cement-based materials leads as well to microstructural heterogeneity changes, with consequent change in the XDFCI signal [65–67]. As a result, XDFCI exhibits high sensitivity to local water water-content changes, since it can visualize regions affected by water-content changes when the majority of the pore space is below the spatial resolution of the imaging system. The latter condition is always the case for cement-based materials because they have a majority of pore space with size at the length scale of tens/hundreds of nm.

The availability of XACI and XPCI images, in addition to XDFCI ones, when using either approach among EI, SPA or TLI, also offers the possibility of exploiting the different types of contrast for better resolving the specimens' microstructural changes occurring at a length scale above the spatial resolution, thus empowering the investigation of the couplings between the microstructural evolution and the water transport at early-ages.

TLI-based XDFCI has been previously used to investigate microstructural changes during

hardening [66] and the release of water from a saturated porous limestone embedded in a cement paste and used as an internal curing element [65].

In this work, we exploited XDFCI, implemented by TLI at the laboratory scale, to investigate early age water displacements with higher temporal and spatial resolutions (191 s and 105 μm, respectively) and higher sensitivity to local water content changes than those achieved by Bentz et al. [1,2]. The object of our investigation was a system made of two mortar layers with distinct w/c values, the top layer being exposed to an environment with lower RH, thus subjected to evaporative drying. As in the work of Bentz et al., we chose such type of specimen as a model system of the spatial heterogeneity in pore size distribution in actual early-age cement-based materials hardening under the simultaneous occurrence of drying shrinkage.

We performed a time-lapse multi-contrast radiography measurement campaign by TLI during hydration of the system. The multi-contrast imaging involved, simultaneously, two other mortar specimens with the same w/c values and boundary conditions, i.e., sealed or open to the environment, of the two respective layers of the model system. We used these two reference mortar specimens to better understand the relative importance of evaporative drying and of the microstructure formation in regulating the water transport, as such to resolve the roles of the two driving processes and their respective weights.

In Section 2, we describe the preparation and characterization of the model system and of its respective reference specimens. We then briefly summarize the image formation mechanisms in TLI and the configuration of our TLI radiography campaign, while we leave the details of the necessary image processing to the Supplementary Materials [99]. We also describe the standard, XACI micro-tomography measurements we performed on the model layered system after the TLI one for characterizing the pore space with better spatial resolution than what achieved by TLI-based XACI. We used these additional pore space data for the validation of the XDFCI results.

In Section 3, we report the results of the qualitative visualization of the spatial-temporal distribution of water inside and across the two distinct layers during cement hydration and evaporative drying and its characterization in terms of the spatial pore space information obtained by 3D image analysis of the XACI micro-tomography data. All the details of how we performed the analysis are contained within the Supplementary Materials [99].

In Section 4, we conclude with a summary of the results obtained, in comparison with those obtained previously by Bentz et al., and we provide an outlook about the advantages of XDFCI for the systematic investigation of early-age processes involving water displacements in cement-based materials.

2. Materials and methods

2.1. Materials and model layered system/reference specimens preparation and their characterization

Three casting molds were produced by 3D printing technology at the Technical University of Munich. The 3D printer was a Stratasys Objet Eden260VS® and the printed material was Stratasys VeroBlackPlus (RGD875), a black and rigid photopolymer-based plastics. The size of the inner horizontal (Z-X plane in Figure 1(a)) cross-section is 6 mm in length (X-axis) × 5 mm in thickness (Z-axis) for all the three molds, with 1-1.5 mm wall thickness. Two of the molds have an inner volume height (along the Y-direction) of 12 mm, the third one of 10 mm. Before preparing the mortar specimens, the three molds were, laterally and at their bottom, sealed with Kapton® tape to reduce water loss by evaporative drying through the possibly not perfectly sealed edges of those lateral surfaces.

Two types of mortars, called M1 and M2 and with different w/c, 0.42 and 0.30 respectively, were used in this study. The mortar mix design is given in Table 1. We used ordinary Portland cement of type CEM I 42.5N. The cement density was 3.15 g cm^{-3} and the Blaine fineness 3190 cm^2 g^{-1}. Alluvial sand with density 2.65 g cm^{-3} and particles size ranging from 250 to 500 μm was employed. The sand content was 40% by volume for both mortars. Polycarboxylate-based superplasticizer (SP) was used for the M2 mortar, at a dosage of 0.8% by mass of cement.

Mortar type	M1 (0.42 w/c)	M2 (0.30 w/c)
Cement CEM I 42.5N (kg/m^3)	821.5	971.3
Aggregate (kg/m^3)	1060.0	1060.0
Water (kg/m^3)	345.0	283.6
SP (kg/m^3)		7.8
w/c	0.42	0.30

Table 1. Mix design of the two mortars (M1 with 0.42 w/c and M2 with 0.30 w/c). For each component, the mass per unit volume of the mixture is provided.

The cement and dry sands were dry-mixed manually, after which either de-ionized water, for the M1 mortar, or the mixture of de-ionized water and SP, for the M2 mortar, was added to the mixture. The mortar preparation was done with a vacuum mixer (Twister Evolution) by Renfert. The overall mixing lasted 2 minutes at the speed of 450 rev/min. The same mixtures used to produce the actual specimens of investigation were mixed again at a later time to perform isothermal calorimetry with a TAM Air Isothermal Calorimeter produced by Thermometric AB. Isothermal calorimetry helped to identify the different stages of hydration of the

mortars, in order to correlate the multi-contrast X-ray radiography results with the information about the hydration kinetics.

The M1 mortar was mixed first. While mixing the M2 mortar, we cast the M1 mortar into the two taller molds. We filled completely one of these two molds to realize a reference M1 specimen. This mold's top was covered with a plastic lid, sealed with grease to reduce as much as possible any water loss due to evaporative drying during the TLI measurements. We filled the other taller mold up to half of its height. The top half volume of this mold was then filled with the M2 mortar, in order to realize the model layered system with the lower w/c mortar on top of the higher w/c mortar. When filling the mold with either mortar layer, we gently tapped it in order to favor a uniform cast and to reduce entrapped air voids as much as possible. The mold for the model system remained open during the overall duration of the TLI measurement, in order to subject the M2 layer to direct evaporative drying through its top surface. During the overall measurement time, the RH and temperature inside the TLI hutch were about 30% and 28-30°C.

The third and shorter mold was completely filled with the M2 mortar only, to realize a reference M2 specimen. The top of this mold was also left open in order to have the same boundary conditions as for the top M2 layer in the model system.

Finally, the three molds were fixed on a plate, side by side along a line orthogonal to the X-ray beam direction (Z-direction in Figure 1(a)) and with their thickness aligned along the beam. The three specimens were not moved from the TLI specimen holder until the end of the experimental campaign. We measured the mass of the three molds before and after the campaign to estimate the water loss due to the evaporative drying.

As done by Bentz et al. [1,2], we chose to investigate such model layered system because it allows investigating early-age water transport in conditions similar to those of interest for practical applications. In particular, a more porous region surrounded by a less porous matrix exposed to the external and drier environment is encountered in the investigation of water release into a mortar matrix by LWAs or SAP particles. Another case of interest is local water transport inside a mortar matrix across regions characterized by different pore size distributions and porosities (which might be intrinsic to real world concrete, e.g., due to inhomogeneities resulting from the casting process or induced by damage).

2.2. Multi-contrast time-lapse X-ray radiography measurement by Talbot-Lau interferometry

Figure 1 shows a layout of the TLI setup at the Technical University of Munich used in this study.

A typical Talbot-Lau interferometer, as the one depicted in Figure 1(b), comprises three gratings, G0, G1 and G2, with line patterns having periodicity at the μm scale, aligned along a single direction, the Y-axis of Figure 1 in our case.

X-ray TLI consists of measuring on a detection plane the changes brought by a specimen to a periodic X-ray interference pattern produced by illuminating, with a highly spatially coherent X-ray beam, a periodic grating (G1 in Figure 1(b), typically called as the "phase" grating) consisting of gaps alternated to a given material thickness, producing a certain phase shift of the beam at a certain energy (Talbot-Lau effect [68,69]). Any local perturbation of the interference pattern is due to the local values of the X-ray complex index of refraction n of the specimen. By resolving the changes in the interference pattern, the linear projections of β, δ and ϵ can be retrieved point-wise from a signal processing procedure described in Section S1 of the Supplementary Materials [99]. The basic physical principles of such retrievals consists of a contribution of β, i.e., of the X-ray attenuation, to decreasing the overall average interference pattern intensity while ϵ, i.e., the (U-)SAXS, contributes to decreasing its oscillation amplitude. δ, i.e., X-ray refraction, contributes to local displacements of the pattern along the direction of the G1 periodicity.

When working with laboratory X-ray sources, which produce beams either spatially incoherent or with very low coherence, a "source" grating, indicated as G0 in Figure 1(b), is placed between the X-ray source and G1, creating an array of mutually incoherent but independently sufficiently coherent beams.

The period of the inference pattern is directly proportional to that of G1. Such period is at the μm scale, in order to achieve sensitivity to spatial variations in n at that scale. In order to be able to resolve the periodic interference pattern created by G1, an X-ray detector with pixel size much smaller than the interference pattern periodicity is needed, which is almost never available, especially at the laboratory scale. These detector technology limitations are overcome by exploiting a third grating, called "analyzer" grating or G2 in Figure 1(b), placed in front of the detector. The relative translation of G2 in respect to G1 along the direction of the gratings periodicity allows resolving the interference pattern intensity at each pixel location on the detector plane. This is achieved by several translation steps, each corresponding to a fraction of the interference pattern period.

One X-ray radiograph is acquired in correspondence of each translation step. The pixel-wise processing of such radiograph, according to a procedure known as "phase stepping protocol" [70,71] and described in Section S1 of the Supplementary Materials [99], leads to three new radiographs, $P_\mu(x,y)$, $\frac{\partial P_\delta}{\partial x}(x,y)$ and $P_\epsilon(x,y)$. (x,y) indicates the pixel position on the detector plane, according to the coordinate system shown in Figure 1. $P_f(x,y)$ indicates the linear projection of the function $f(x',y',z')$, i.e., a path integral of $f(x',y',z')$ along a ray connecting the source and the position (x,y) on the detector plane.

The phase stepping protocol requires two sets of radiographic acquisitions, one in the absence (reference scan) and the other in the presence of the specimen. We refer to Section S1 of the Supplementary Materials for the complete description of the image processing leading to the

retrieval of the three radiographs $P_\mu(x,y)$, $\frac{\partial P_\delta}{\partial x}(x,y)$ and $P_\epsilon(x,y)$. In this study only $P_\mu(x,y)$ and $P_\epsilon(x,y)$ were used [99].

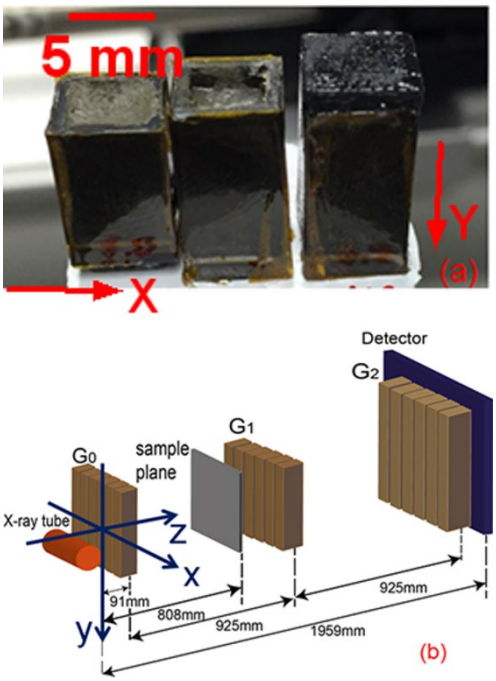

Figure 1 (with colors in the online version of the article). (a) Picture of the three 3D printed molds with the mortars cast inside them, just before being mounted of the specimen stage of the X-ray imaging setup. The M2 reference specimen is on the left side while the M1 (with its top sealed by a lid) on the right. The layered specimen is the one in the center. (b) Schematics of the X-ray Talbot-Lau interferometer at the Technical University of Munich, with the geometric settings used in this study. The X-ray source was located at the Z = 0 mm plane. The zoom-in window on top of the specimen plane shows the picture of the three specimens during the experiment.

The three gratings of the Talbot-Lau interferometer used in this study were set according to the distances shown in Figure 1(b) such that the interference pattern was created at the first fractional Talbot-distance of the interferometer (distance between G1 and G2). The G0 and G2 gratings were of the same type, with period of 10 μm and made of gold as material filler of the gaps, with thickness of 150-170 μm along the beam direction. G1 had a period of 5 μm and was made of Ni, with thickness of 8 μm along the beam direction, leading to a $\pi/2$ phase-shift of the illuminating beam at 45 keV. The X-ray source was a micro-focus source produced by X-ray WorX (Garbsen, Germany) of type XWT-160 SE. It was operated at 60 kV_{max} and ≅680 μA in order to achieve an energy spectrum with mean value of 45 keV. With this configuration, a mean TLI visibility (see Section S1 of the Supplementary Materials for its definition [99]) of 22.9% was obtained in a central region of the field of view (FOV). The X-ray detector was a PaxScan 2520DX by Varian, with physical pixel size p = 127 μm and 1920×1536 pixels (X and Y directions of Figure 1, respectively), based upon a 600 μm-thick CsI scintillator screen, for the conversion of X-ray photons to visible light photons, on top of

an amorphous Si as direct converter of visible light photons to electrical charge. The detector readout was set to 1 frame per second so that several images were acquired and pixel-wise averaged to produce a final radiograph with higher signal-to-noise ratio within the single radiograph acquisition time.

The micro-focus X-ray source produced a cone beam with correspondent projection magnification factor $M = \frac{d_{SD}}{d_{Ss}} \cong 2.42$ and effective pixel size $\tilde{p} = \frac{p}{M} \cong 52.5\ \mu$m, where d_{SD}=1959 mm was the source-to-detector distance while d_{Ss}=808 mm was the source-to-specimen distance. We estimated an effective average spatial resolution in the radiograph of the order of double the effective pixel size (105 μm).

2.3. *Radiographs acquisition and processing*

As soon as we fixed the specimen on the specimen holder, we immediately started the acquisition of the radiographs by TLI, following the protocol described below.

First, the specimens were moved out of the FOV to perform a reference phase stepping protocol consisting of 8 steps with equidistant displacement over 1 period of the interference pattern, equal to the period of G0(G2) ($\cong$10 μm). Then the specimens were moved back into the FOV and the same phase stepping protocol was repeated once. After that, the specimens were moved out of FOV again and the whole procedure was repeated (1 reference phase stepping protocol + 1 specimen phase stepping protocol). A reference phase stepping protocol was needed before each specimen's in order to perform the TLI signal processing (Section S1 of the Supplementary Materials [99]), at each time point, with reference interference patterns as closely related as possible to the actual ones illuminating the specimen. Such reference patterns can vary significantly in time due, e.g., to temporal fluctuations of the X-ray source.

At each step of any phase stepping protocol, each radiograph was acquired with an exposure time of 8 seconds (8-frame averaging). The temporal resolution of the multi-contrast time-lapse radiography campaign was 191 s, considering the total acquisition time for each radiograph at each phase stepping stage, the time for the stepping for each of the two cycles of the phase stepping protocol, in the absence and in the presence of the specimens, and the time needed to move them out of and into the FOV. Thus, after retrieval, one $P_\mu(x,y)$ radiograph, one $\frac{\partial P_\delta}{\partial x}(x,y)$ and one $P_\epsilon(x,y)$ were obtained every 191 seconds. The overall campaign lasted approximately 7 h continuously, consisting totally of 133 reference phase stepping protocols and respective 133 specimen ones, thus 133 multi-contrast radiographs.

2.5. X-ray attenuation contrast micro-tomography analysis of the pore space

We performed attenuation-contrast X-ray micro-tomography only on the model layered system at Empa's Center for X-ray Analytics (http://www.empa.ch/web/s499/mct) for quantitatively analyzing the resolvable part of its pore space and for supporting the interpretation of

the water transport spatial-temporal patterns observed by the time-series of dark-field contrast radiographs.

A micro-focus X-ray transmission source, manufactured by VISCOM AG (Germany, type XT9160 TXD), based upon a tungsten target and with focal spot size of ≅ 2-3 μm, was used and operated at 80 kV_{max} and 120 μA.

The X-ray detector was a digital flat-panel detector of type XRD 1621 CN2 ES from Perkin Elmer (United States) with a 0.7 mm-thick tallium–doped cesium iodide CsI(Tl) scintillator screen, for the conversion of the X-ray photons to the visible light ones, and amorphous Si pixels for the direct conversion of the visible light into electric charge. The physical pixel size is p_{micro}=200 μm. The FOV consisted of 2048×2048 pixels. The source-to-detector distance was $d_{SD,micro}$= 1017 mm while the source-to-specimen distance was $d_{Ss,micro}$= 35 mm, leading to a projection magnification factor $M_{micro} \equiv \frac{d_{SD,micro}}{d_{Ss,micro}} \cong 29$ and an effective voxel size $v_{micro} = \frac{p_{micro}}{M_{micro}} \cong 6.9$ μm. The spatial resolution of the final tomogram was thus estimated of the order of 14 μm.

The micro-tomography measurement consisted of 2000 radiographs acquired over a range of 360° of relative orientation of the specimen around an axis parallel to the vertical axis of the detector plane. The radiograph at each orientation angle was the result of acquiring and averaging five of them with 900 ms as acquisition time per radiograph.

The radiographs recorded were corrected for the dark-current and flat field by a detector calibration procedure. The overall measurement took 3 h 46 min. The raw radiographs were saved as 16 bit unsigned integer images.

The tomographic reconstruction was performed with the tomographic reconstruction software Octopus Reconstruction® (XRE, Belgium), using a standard filtered back-projection algorithm for a cone beam geometry [72], optimized for GPU processing. After reconstruction, the horizontal (X-Z) cross-sections of the reconstructed 3D spatial distribution of $\mu(x', y', z')$ (attenuation-contrast tomogram) were saved as floating-point 32 bit images.

The 3D image processing implemented for segmenting and characterizing the pore space above the spatial resolution of the tomogram is described in details in Section S4 of the Supplementary Materials [99].

3. Results and discussion

3.1. Hydration kinetics by isothermal calorimetry

The rate of heat release (or heat flow) due to cement hydration, for both reference mortars M1 (w/c = 0.42) and M2 (w/c = 0.30), is reported in Section S3, Figure S2, of the Supplementary Materials [99]. The goal of these measurements was to estimate the time of initial and final set

of the two mortars, to be compared with the time scale of the multi-contrast radiography campaign (7 hours).

The calorimetry results show that within the first 7 hours of hydration, corresponding to the same duration of the multi-contrast time-lapse radiography campaign, the initial setting of both mortars and likely also the final setting for mortar M1 were completed, while both mortars approached the conclusion of their acceleration periods within the time range of 9-10 hours. The results suggest that most of the relevant microstructure evolution of both mortars occurred before the end of the radiography campaign.

Thus, the results of the radiography campaign, presented in the following Section, deal with the visualization of water transport during the most significant time interval of the microstructure formation.

3.2. Multi-contrast time-lapse radiography by Talbot-Lau interferometry during hydration and evaporative drying

Figure 2 shows the dark-field contrast radiographs, $P_\varepsilon(x, y, t)$, where t means time, (insets (a), (b), (c), left column), and the attenuation contrast radiographs, $P_\mu(x, y, t)$, (insets (d), (e), (f), right column), at three different time instants during the campaign (rows). The left column images show the values of $P_\varepsilon(x, y, t)$ in units of 10^{-12}, with brighter pixels indicating larger cumulative (U-)SAXS "strength", while the right column images show the $P_\mu(x, y, t)$ values, with brighter pixels associated with more X-ray attenuating regions. For each contrast type, the dynamic range of the shown images was identically set for each time instant, for more reliable visualization of the temporal changes and their proper comparison. The rectangles drawn inside each specimen in Figures 2(a) to (c) indicate regions of interest (ROIs) over which, at any time instant during the campaign, $P_\varepsilon(x, y, t)$ was spatially averaged, to obtain a "dark-field contrast signal" $S_i(t) = \langle P_\varepsilon(x, y, t)\rangle_{(x,y)_i}$, where the index i identifies the ROI and the symbol $\langle \dots \rangle_{(x,y)_i}$ indicates the pixel-wise averaging over the ROI i. The same ROIs were defined and used to perform similar averaging also for the attenuation contrast radiographs, computing for each ROI i a corresponding "attenuation contrast signal" $A_i(t) = \langle P_\mu(x, y, t)\rangle_{(x,y)_i}$. Important to notice in Figure 2 is that the ROIs for the reference M1 and M2 specimens covered approximately their entire heights while, for the layered specimen, each of the two ROIs covered approximately either the M1 layer at the bottom or the M2 one at the top, respectively. Such span for any ROI on any specimen was chosen as such to track only the bulk temporal evolution of the attenuation and dark-field contrast signals during the ongoing hydration and drying, without being influenced by fluctuations due to localized spatial differences.

The change, for the attenuation radiographs, inside any specimen and during the overall measurement, is hardly visible by the naked eye in Figure 2. The spatially averaged pixel values only slightly decreased with time, with a more appreciable decrease for the reference M2

specimen on the right side of the radiographs and the top M2 layer in the model system center specimen. A slightly better visual evidence of such a decrease is obtained by looking at the whole time series of attenuation radiographs, available in the form of a movie in Section S5 of the Supplementary Materials [99].

In contrast, a clear evolution is visually easily appreciable for the dark-field radiographs, with qualitative differences in behavior for the M1 reference specimen and the M1 (bottom) layer in the model system while the M2 reference specimen and the M2 (top) layer of the model system qualitatively behave the same.

Such differences/similarities result from the distinct phenomena happening within the distinct specimens. The M1 reference specimen (left in each radiograph), subject to almost no evaporative drying because of the top sealing of its mold, exhibited a gradual and small decrease in P_ε. On the contrary, the M2 reference mortar (right in each radiograph) showed an increase in P_ε followed by the achievement of a plateau level (no large change is visible between Figures 2(b) and (c) for that specimen). In the model layered system (center in each radiograph), P_ε looks like having increased in both the top M2 layer and in the bottom M1 layer. However, a larger increase seems to have happened in the M2 layer than in the M1 one.

These qualitative observations and conclusions are better validated also by the visual inspection of the complete time series of dark-field and attenuation contrast radiographs, reported and described in Section S5 of the Supplementary Materials [99].

One last note regarding Figure 2 concerns a feature observed at any time instant in the M2 reference (right) specimen dark-field radiographs. An irregular, "crack"-like feature with low P_ε value is visible on the left side of the specimen. This was an artificial feature created in such radiographs and at that location by a physical scratch on the G1 grating, which introduced an artifact only within the $P_\varepsilon(x, y, t)$ and $\frac{\partial P_\delta}{\partial x}(x, y)$ radiographs.

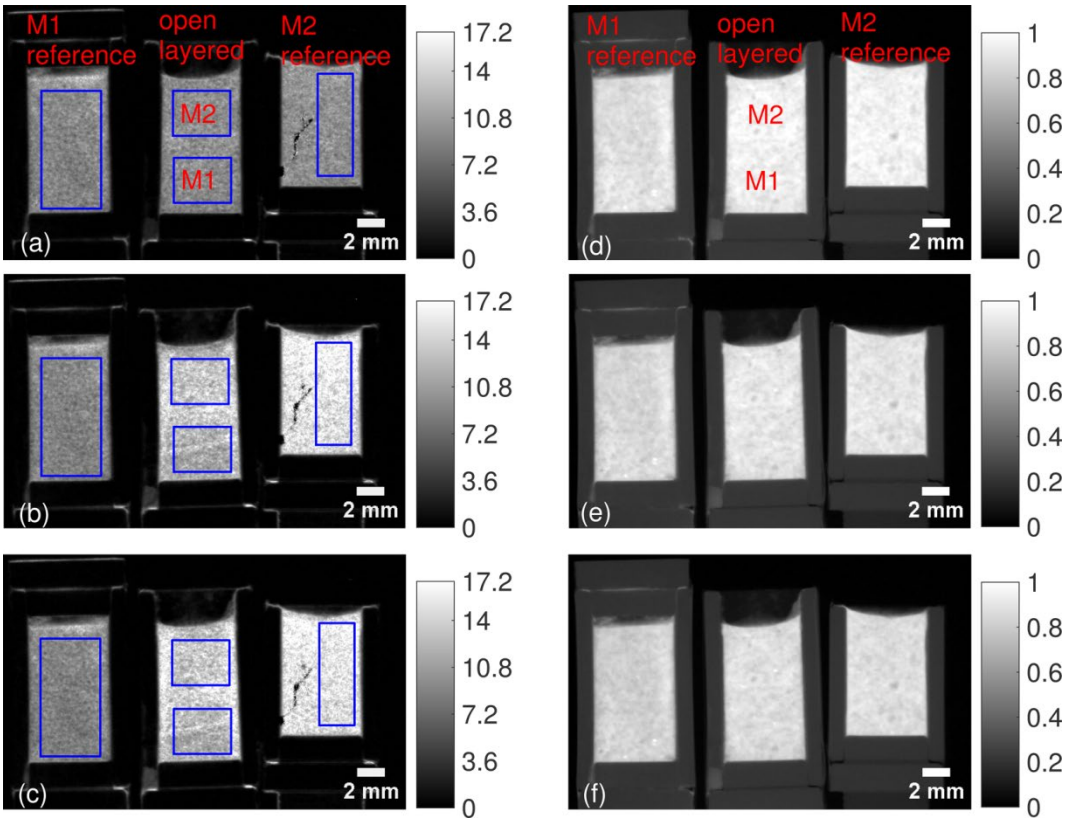

Figure 2 (with colors in the online version of the article). Dark-field, $P_\varepsilon(x, y, t)$, ((a), (b), (c)) and attenuation, $P_\mu(x, y, t)$, ((d), (e), (f)) contrast radiographs at three different time instants, t_0 (beginning of the campaign, (a) and (d)), t_1 (after 2 hours and 54 minutes, (b) and (e)) and t_2 (close to the end of the campaign, after 6 hours and 58 minutes, (c) and (f)). The dark-field contrast radiograph pixel values are reported as multiples of 10^{-12}. Superimposed on the dark-field radiographs are rectangular regions of interest (ROIs) which were used to calculate, for each specimen, the spatially averaged linear projection of the (U-)SAXS "strength", $\langle P_\varepsilon(x, y, t)\rangle_{(x,y)}$, as a function of time (see Figure 3). The ROIs were, for each specimen, the same at each time instant.

A quantitative validation of the conclusions drawn before and regarding the temporal evolution of P_ε in the different specimens is provided by its pixel-wise average values over the different ROIs highlighted by the rectangles in Figure 2. Figure 3 reports such dark-field contrast signals $S_i(t)$ after their normalization by each respective signal value at the beginning of the experimental campaign, i.e., it shows $\tilde{S}_i(t) \equiv \frac{S_i(t)}{S_i(t_0)}$. We call this signal the normalized dark-field contrast signal.

Figure 4 reports a correspondingly normalized attenuation contrast signal $\tilde{A}_i(t) \equiv \frac{A_i(t)}{A_i(t_0)}$ for the same ROIs.

At the basis of our interpretation of the results reported in Figure 3, there is the assumption that the mold of any specimen was perfectly sealed, except for the opening to air at its top, for the model layered system and the reference M2 mortar.

The mass of each specimen was measured before and after the experiment in order to assess the extent of validity of such assumption. The results are reported in Table 2. While some lim-

ited mass loss was recorded also for the M1 specimen (nominally sealed), this was, as expected, much smaller than for the unsealed specimens (more than 4 times smaller). Moreover, one should take also into account that the absolute mass changes were very small (in the order of a few 1/100 of g) for each specimen. We hypothesize that a mass loss, although very small, occurred systematically, with the sealed reference M1 specimen as well with the other two, because during handling each specimen could have possibly lost some of the grease applied to seal it. We thus attribute the rest of mass loss for each unsealed specimen to the evaporative drying through the top, open surface.

	Before measurement m_{before} [g]	After measurement m_{after} [g]	Relative mass change $((m_{after} - m_{before})/m_{before})$ [%]
M1, reference+ tube	1.5816	1.5689	-0.80%
M2, reference+tube	1.2506	1.2025	-3.85%
M1+M2, layered+tube	1.3631	1.3116	-3.78%

Table 2. Mass of each specimen before and after the measurement and relative mass change.

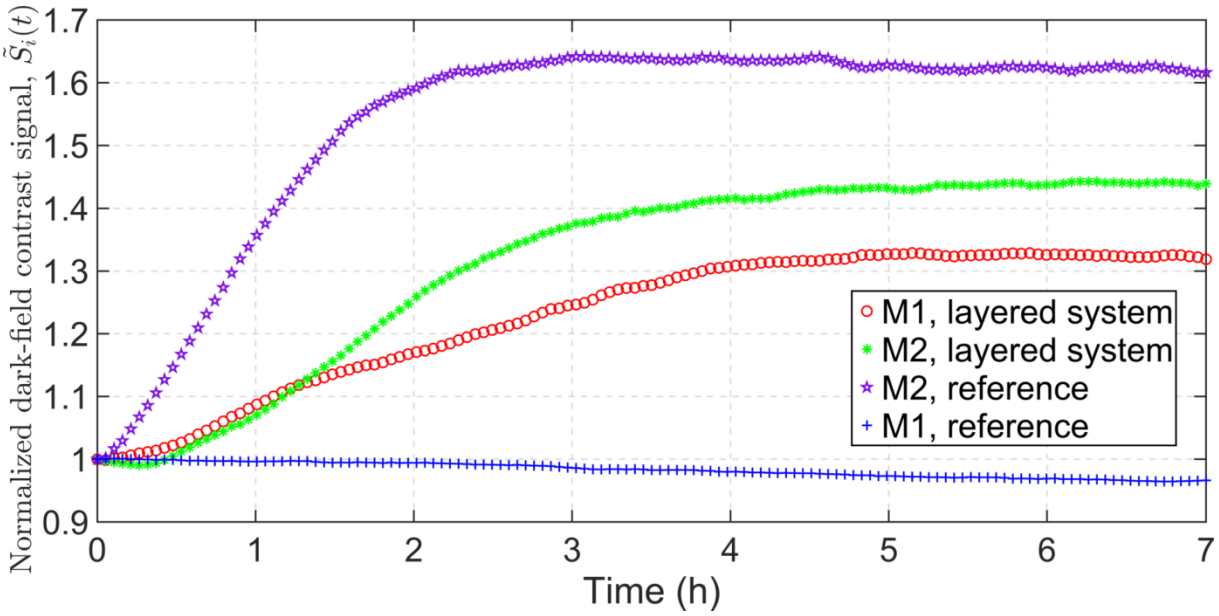

Figure 3 (with colors in the online version of the article). Temporal evolution, during the overall multi-contrast radiography campaign, of the pixel-wise average value, $S_i(t) = \langle P_\varepsilon(x,y,t)\rangle_{(x,y)_i}$, of the linear projection P_ε of the (U-)SAXS "strength", ε, normalized by the same average value at the beginning of the measurement campaign, $S_i(t_0)$ ($t_0 = 0$ hours). Such average values are also called normalized dark-field contrast signals and are indicated as $\tilde{S}_i(t)$, where the integer index i just enumerates them. Different curves refer to distinct regions of interest (ROIs), highlighted as rectangles in Figures 2(a)-(c) and covering the different specimens or parts thereof: M1, bottom layer in the model system (red circles); M2, top layer in the model system (green asterisk); M2 reference specimen (purple pentagram); M1 reference specimen (blue plus sign).

Figure 3 confirms that the cumulative (U-)SAXS "strength" monotonically decreased during the overall campaign for the M1 reference specimen, even though within a small range (the relative change between the beginning and the end of the campaign was $\Delta\tilde{S}$ =-3.47%).

Cement hydration and the corresponding microstructure formation lead to the creation of the hydration products network. In the absence of evaporative drying, two main features of such formation may influence differently the evolution of the real part of the X-ray index of refraction, δ, local values, thus of the normalized dark-field contrast signal $\tilde{S}(t)$.

On the one side, chemical shrinkage and the corresponding emptying of capillary pores should contribute to an increase in the local scattering of the X-ray photons, thus to an increase in the macroscopic (U-)SAXS "strength" measured by TLI. That is because the emptying of such pores increases the interface area characterized by the highest difference in δ value, i.e., the interface between solid material phases and air. Thus the amount of interface area producing strong scattering increases. Such increase occurs at a length scale well below the spatial resolution of the TLI instrument (scale of 100 μm in this work), thus manifesting itself as an increase for the probability of occurrence of the bulk scattering along each ray connecting the X-ray source with a detector's pixel. An increase in such probability corresponds quantitatively to an increase in the macroscopic scattering cross-section Σ, to which the dark-field radiograph pixel value directly and positively relates.

The increase in interface area equipped with the largest possible difference in δ values corresponds, in terms of what measurable in traditional, single point (U-)SAXS experiments, to an increase in X-ray scattering contrast $|\Delta\rho_e|$, where ρ_e means electron density and its difference is taken between the value of the solid phases, e.g., of calcium silicate hydrates, and of the pore fluid, i.e., air in the case of the largest possible achievable value. We notice that the scattered intensity measured in traditional, single point (U-)SAXS measurements scales with $|\Delta\rho_e|^2$, thus chemical shrinkage alone should lead to an increase in scattered intensity [73–76].

On the other side, the growth of the cement hydration products and the correspondingly increasing spatial percolation of their network lead to a gradual refinement of the capillary pores, which become on average smaller and more homogeneously distributed. Another effect of the increasing spatial percolation of the solid hydration products is their increasing spatial packing and "densification".

Together, smaller and more homogeneously-distributed capillary pores, even though they become partially empty due to chemical shrinkage, and more percolating solid phase structures should contribute to a decrease in (U-)SAXS.

The continuous decrease in (U-)SAXS "strength" we observed for the sealed M1 reference specimen is in agreement with what already reported by Prade et al. for the hydration of Portland cement pastes in completely sealed molds and in the absence of any curing agent [66]. Such experimental evidence, together with what presented in this work, suggests that the sec-

ond mechanism, i.e., the reduction of the sub-resolution heterogeneity due to the hydration products network growth, overcomes the first one, in terms of contribution to the cumulative (U-)SAXS behavior, thus to the overall normalized dark-field contrast signal $\tilde{S}(t)$. This is the conclusion we reach for the sealed reference specimen M1, based on the results presented here and on those shown in [66].

Such conclusion is supported by results from both traditional, single point SAXS [73,74] and small angle neutron scattering (SANS) experiments [75,76] reported in the literature and concerning ordinary Portland cement pastes hydrating in sealed conditions.

Single point small angle scattering (SAS) measurements, with either X-rays or neutrons, have been extensively used to characterize the temporal evolution of hydrating cement microstructures in terms of the morphological and structural characteristics of the most abundant cement hydration products (mainly the amorphous calcium silicate hydrates). Allen and Thomas provide an extensive review of what achieved with SANS [77].

Among all the work reported in the literature, that of Kriechbaum et al. about SAXS measurements [73,74] and of Häussler et al. about SANS ones [75,76] is of particular importance for the validation of our conclusion mentioned above, because of the consistency of the results there presented and of the higher similarity of their specimens with ours, when compared with other published work.

Both Kriechbaum et al. and Häussler et al. performed time-lapsed, single point SAS measurements on hydrating cement pastes in sealed conditions with w/c values (0.5 in [73] and 0.38 in [75,76]) close to the ones used in our work (0.42 and 0.3 for M1 and M2, respectively). Their measurements also covered scattering vector magnitude (q) ranges overlapping with each other ([0.3;0.7] nm^{-1} in [73,74], [0.086;1.5] nm^{-1} in [75] and [0.1;1] nm^{-1} in [76]). This common feature implies that the scattering patterns measured in all those works were produced by microstructural changes occurring at overlapping length scale ranges, of the order of [0.67;12] nm (estimated as the reciprocal of the maximum and minimum q values reported above). This feature thus implies high comparability of their results and more reliability of the respective conclusions.

A direct and similar assessment of the exact length scale range at which the microstructural changes affected the normalized dark-field contrast signal $\tilde{S}(t)$ is not feasible when a single configuration of the Talbot-Lau interferometer is used. As mentioned before, TLI does not provide the exact identical information as single-point SAS measurements do, i.e., the dependence between the differential macroscopic scattering cross-section, $\frac{d\Sigma}{d\Omega}$, and the scattering vector magnitude q. Here Ω indicates the solid angle around each scattering direction.

If multiple TLI measurements are successively performed changing the interferometer configuration, specifically the relative position between the specimen and the G0 or G2 gratings (depending on whether the specimen is set in front or behind the G1 grating, respectively), then, as reported in Section 1, the dark-field contrast signal, at any given time, can allow re-

trieving the linear projection, along the beam direction, of the auto-correlation function of the sub-resolution heterogeneity, $G(\zeta_{interf})$, at multiple values of the variable ζ_{interf} [62–64]. We recall that the latter, with the physical dimension of a length, plays the role of a (correlation) length scale, thus the same role as played by q^{-1} in single point (U-)SAXS and SANS measurements. We also recall that ζ_{interf} depends only from the interferometer configuration, specifically on the G0-specimen or G2-specimen distance, on the interferometer design energy and on the period of the G0 or G2 gratings [62–64].

In the absence of multiple TLI measurements by varying ζ_{interf}, we can only estimate for our measurements an upper bound for q and an indicative most probable value (maximum of its probability density function).

The upper bound for q can be quantified by considering its theoretical upper bound computed at the interferometer's design energy of 45 keV.

The theoretical upper bound of q, under the assumption of elastic scattering, is given by $q_{max} = \frac{2E_v}{\hbar c_0}$, where E_v is the photon energy, $\hbar$ is the reduced Planck constant and c_0 is the speed of light in vacuum. By plugging in that equation the interferometer design energy as value for E_v and using an estimate of 0.197 keV · nm for the universal constant $\hbar c_0$, the approximate estimate of the upper bound of q spanned in our experiments is $q_{max} \cong 457$ nm^{-1}, corresponding to a lower bound for the length scale $(q^{-1})_{min} \cong 0.027$ nm.

Such estimate for the (U-)SAXS leading to the dark-field contrast in our measurements has limited usefulness because it reports only the theoretical upper bound, approachable in a wide-angle scattering (WAS) measurement configuration, positioning the X-ray detector at large angles compared with the beam incident on the specimen. On the opposite, the Talbot-Lau interference pattern is not only recorded by a plane detector whose orthogonal direction is parallel to the incident been. The detector is also located at a rather small distance from the object compared with the far Fraunhofer diffraction range. In these conditions, what mostly contributes to the generation of the dark-field contrast is the ultra-small angle component of the overall SAS process, i.e., scattering at very small q values. Thus the lower bound of q, q_{min}, would be a more useful quantity to estimate for comparison with the q ranges within which the SAXS and SANS results of Kriechbaum et al and Häussler et al. were obtained. Such estimation would require performing traditional USAXS measurements on the same specimens of this study and at photon energy equal to the TLI design energy of 45 keV.

In the absence of such quantitative measurements, we can use the value of ζ_{interf} for our TLI configuration as an estimate of the most probable value of q^{-1} at which the dark-field contrast was produced by the (U-)SAXS process.

Figure 1 shows that the specimen was located in front of the grating G1 along the beam direction. In such a configuration, $\zeta_{interf} = hc_0 \frac{d_{G0-S}}{E_v p_0}$ [63], where d_{G0-S} is the G0-specimen distance (=717 mm, Fig. 1), $p_0 = 10\ \mu m$ is the period of G0 and $E_v = 45$ keV is the photon en-

ergy, assumed equal to the interferometer design energy. Under this assumption, $\zeta_{interf} \cong 2\ \mu m$.

Based on this approximate calculation and the hypothesis of ζ_{interf} approximating the most probable value of q^{-1}, we can conclude that the changes in dark-field contrast for the M1 specimen, as well for the other specimens, should have stemmed from the cumulative, bulk microstructural changes mainly or up to such length scales rather than only at the scales of the nano-pores.

The first major result from the SAS measurements by Kriechbaum et al. and Häussler et al. was the systematic observation of a power law scaling of $\frac{d\Sigma}{d\Omega}$ with q of the type q^{α}, with α being a non-integer number and $-4 < \alpha < -2$.

Such power law scaling has been attributed to microstructures having fractal properties [75]: either a volume fractal, when $-3 < \alpha < -2$, or a surface fractal, when $-4 < \alpha < -3$. In the former case, $|\alpha| = D_V$, the volume fractal dimension. In the latter case, $|\alpha| = 6 - D_S$, where D_S is the surface fractal dimension.

SANS studies by Allen et al. have attributed to the disordered packings and networks of outer, lower density calcium silicate hydrate particles the resemblance with volume fractals generated in numerical simulations of diffusion-limited particle aggregation processes [78]. The same studies have attributed to the calcium silicate hydrates forming directly on top of the interface between clinker particles and capillary pores resemblance with surface fractals.

Fractal geometry properties, either volumetric or surface ones, of the calcium silicate hydrates, as evinced from SAS measurements, provide a formalized and quantitative characterization of such hydrates mirroring what both qualitatively and quantitatively [99] observed by transmission electron microscopy [80] and soft X-ray ptychography [81], i.e., the tendency of the hydration products to have high degrees of convolution, folding and space filling.

The second major result in the studies by both Kriechbaum et al. and by Häussler et al. consists in the systematic observation of an increase in the $|\alpha|$ with increasing hydration age. Depending on the q ranges, corresponding to either $-3 < \alpha < -2$ or $-4 < \alpha < -3$, i.e., either to volume or to surface fractal scattering behavior, an increase in $|\alpha|$ implies an increase in D_V towards a value of 3 or a decrease in D_S towards a value of 2, respectively. Such values correspond to the topological dimensions of a volumetric object or of a surface one, respectively, embedded in 3D and not-being fractal [77,78,82]. Thus, in either case, a temporal increase in $|\alpha|$, during hydration and in the absence of evaporative drying, signals a decrease in fractal geometry properties as a consequence of a continuous evolution from an open and ramified percolating network of hydration products to a more closed and more compact one, with more homogeneously distributed and more refined empty capillary pores, as mentioned above.

Those observations by single-point SAXS and SANS measurements are thus compatible with the hypothesis we make in this work based upon our observations of a decrease in the bulk and normalized dark-field contrast signal $\tilde{S}(t)$ for the sealed reference specimen M1.

The radiography campaign lasted about seven hours, during which the cement hydration process was still within the acceleration period. Thus we expect that the normalized dark-field contrast signal $\tilde{S}$ could have continued to decrease, reaching a plateau only after the beginning of or well into the deceleration period, as a consequence of the slow-down in the hydration products' volume ratio increase.

Compared with the results obtained by Prade et al. within a similar time scale (7 hours hydration) with a Portland cement paste with lower w/c value (0.312), we observed for the hydration of our M1 reference mortar (w/c = 0.42) a much lower relative decrease in the normalized dark-field signal (about 3.5% against 27%, in absolute value) [66]. This difference might be explained by the fact that mortar and not cement paste was measured in the present study contrary to what done in [66]. The aggregates would both "dilute" the change in the $\tilde{S}$ signal and lead to different pore structure properties. In addition, the capillary pore size distribution in the two systems differed due to the w/c. Despite such difference in magnitude of the (U-)SAXS "strength" decrease, our results for the reference mortar M1, hydrating in sealed conditions, confirm the qualitative trend of the dark-field contrast signal as observed previously by Prade et al. [65,66] and agrees with the interpretation of the temporal evolution of microstructural parameters obtained by single point SAXS and SANS measurements on hydrating and sealed cement pastes [73–76].

A completely different dark-field contrast behavior was observed for the M2 reference specimen, whose normalized dark-field contrast signal increased with time within the first three hours of hydration up to a plateau value about which it fluctuated for the rest of the campaign. Such an increase suggests that the main additional process taking place in this specimen, i.e., evaporative drying, overcame the hydration products formation in determining the degree of sub-resolution heterogeneity. While the latter process contributes to decreasing such heterogeneity, thus the dark-field contrast, evaporative drying empties capillary pores and air voids, (while chemical shrinkage only empties the capillary pores or only part of them), contributing to an increase of the sub-resolution heterogeneity, thus of the dark-field contrast.

Pore emptying, as explained before, increases the scattering contrast $|\Delta\rho_e|$. However, it also leads to additional microstructural modifications of the hydration products which amplify the normalized dark-field contrast signal increase shown in our work.

Some of these microstructural changes have been investigated by traditional, single point SANS and SAXS measurements on cement pastes subjected to evaporative drying not immediately after demolding but after a certain number of days/years, when the hydration degree can be considered having almost or completely achieved its maximum possible value. The advantage of using specimens with almost completed hydration consists in the possibility of

836 better observing, as mirrored in scattering changes, only the poro-mechanical and microstruc-
837 tural effects of a decrease in saturation degree upon drying. In that case, the interpretation of
838 such changes becomes easier because hydration products growth does not play anymore a
839 role.

840 Thomas et al. performed SANS measurements within the q range [0.02;2] nm^{-1} , i.e., a length
841 scale range of [0.5;50] nm, on white Portland cement pastes subjected to evaporative drying at
842 distinct and successively decreasing RH values starting either at 8 days or at 3 years of curing
843 by submersion into a $Ca(OH)_2$ solution [83]. Similar trends for the SANS curves with de-
844 creasing RH values were obtained for both types of specimens, suggesting that for such ce-
845 ment paste the maximum hydration degree was already approached, if not completely
846 achieved, before or at 8 days from casting.

847 The authors of that work mention that a unequivocal quantification of changes, with drying,
848 for the maximum value of the neutron scattering contrast, $|\Delta\rho_n|$, was not feasible because at
849 distinct RH values three material phases, i.e., the solid hydrates, liquid water and air in the ca-
850 pillary and larger pores, contributes differently to the macroscopic, effective values of $|\Delta\rho_n|$.
851 Thus a unique trend of $|\Delta\rho_n|$ with drying could not be obtained. However, they could observe
852 the same type of scaling relations between $\frac{d\Sigma}{d\Omega}$ with q, i.e., $\frac{d\Sigma}{d\Omega} \propto q^{\alpha}$, characteristic, at distinct q
853 ranges, of either surface or volume fractals. In addition, by fitting of such scaling relations
854 with a model function [78], they could quantify the temporal evolution, with drying, of sever-
855 al parameters with direct microstructural meaning, among which the volume fractal dimen-
856 sion D_V, the surface fractal dimension D_S and the total internal surface area, S_{tot}. Some of
857 these results provide possible additional explanations for the increase in normalized dark-field
858 contrast signal observed in our work.

859 At any RH value, Thomas et al. obtained values for D_V smaller than 3 (between 2.45 and 2.7)
860 and values for D_S larger than 2 (between 2.1 and 2.5). Such values clearly provide evidence of
861 fractal geometry features from the porous microstructure within the length scale range of
862 measurement ([0.5; 50] nm).

863 Regarding the temporal evolution with drying, Thomas et al. reported a small variation in D_V,
864 especially below 54% RH, interpretable as an increase in volumetric fractal properties. The
865 surface fractal properties also increased with drying but only up to 54% RH and much more
866 significantly than the volumetric fractal properties did. They correspondingly observed an in-
867 crease in scattered intensity within the q range relating with the surface fractal components at
868 the probed length scale. Finally, the estimated total internal surface S_{tot} monotonically de-
869 creased with drying.

870 Thomas et al. interpreted all of these observations in terms of a systematic increase in packing
871 of the cement hydrates particles caused by increasing capillary forces generated by evapora-
872 tive drying. This type of packing should lead to a densification of the hydrates, especially of
873 the calcium silicates ones, without a refinement of the capillary pores as occurring during the

hydrates growth. On the contrary, according to Thomas et al., it should contribute to creating new porosity because of the counter-action of the restraint exercised by the other solid phases, e.g., $Ca(OH)_2$, with less tendency to shrink than the calcium silicate hydrates. This newly created porosity should also increase the scattering due to the interfaces between the hydrates directly decorating the surface of the clinker particles and air, thus increasing the surface fractal properties sensed by the probing radiation.

We hypothesize that this set of mechanisms should be more accentuated in a mortar than in a cement paste, due to a higher volume fraction of phases, e.g. fine aggregates, with shrinking tendency smaller than that calcium silicate hydrates. As a consequence, the production of new, empty porosity should be expected to additionally occur also at larger length scales, i.e., smaller q values, than what observable with point-like SANS and SAXS measurements, leading to the bulk increase in dark-field contrast as observed in Fig. 3.

Below 54% RH, Thomas et al. observed a decrease in D_S towards values closer to the non-fractal one (2), as if the packing of calcium silicate hydrates stopped or decreased. They interpreted such result in terms of lower stability of water-air interfaces at such lower RH values, reducing the magnitude of the corresponding capillary forces instead of increasing them as it should be expected by the Kelvin and Young-Laplace laws [83].

Finally, Thomas et al. interpreted the monotonic decrease in total internal surface area, S_{tot}, as a direct consequence of the calcium silicate hydrates shrinkage and packing, which should have increased the contact area between their particles. This last interpretation agrees with estimates of internal surface area obtained by Beddoe and Lang with single point SAXS measurements on hardened cement pastes undergoing drying [84]. Such surface area decrease, considered alone, should suggest a decrease in normalized dark-field contrast signal instead of the observed increase, unless such surface area mainly belongs to interfaces between solid phases and liquid water, either free or adsorbed, in which case its loss would be less affecting the bulk dark-field contrast stemming from the interfaces between solids and empty pores at larger length scales.

Overall we hypothesize that the cracking resulting from the calcium silicate hydrates' shrinkage proposed by Thomas et al. based upon their single point SANS measurements should have occurred in our M2 reference and M2 top layer specimens, as well as in the M1 bottom layer one, in a sort of amplified way compared with what obtainable in a cement paste only. That should have occurred because of the larger volume fraction of solid phases acting as restraints (the aggregates) and also because of drying occurring while hydration was still ongoing, thus in the presence of a less cohesive and interconnected or even less percolated hydration products packings. As a consequence of more shrinkage cracking, we also expect a larger increase in normalized dark-field contrast signal for an hydrating and drying mortar than for a cement paste, as it has been shown that micro-cracks enhance the dark-field contrast [85].

The hypothesis of larger early-age shrinkage cracking at micron scale for mortars than for cement pastes is also in agreement with the larger amount of overall macroscopic drying shrinkage and cracking measured for mortar specimens subjected to drying [86,87].

Such hypothesis could be tested by performing similar measurements as reported in this work but with a cement paste specimen, instead of a mortar, cast with the same w/c value and same raw materials. According to this line of thinking, we would expect to observe a smaller or slower increase in the normalized dark-field contrast signal.

The formation of new porosity, in the form of micro-cracks, at larger size ranges than just at the scale of capillary pores, as hypothesized by Thomas et al. for their cement specimens, is compatible with the increase of the normalized dark-field contrast signal and would be compatible with an increase in surface fractal dimension D_S, which could be estimated by performing single point USAXS measurements. We would like to carefully remark here that, as the estimated value ζ_{interf} shows, it would be necessary to perform USAXS and not SAXS measurements, as such to probe the microstructural changes up to length scales of tens of microns. Only in this case, the USAXS results could provide useful information to support the interpretation of the dark-field contrast ones obtained from TLI.

Regarding the model layered system, in the absence of any water displacement from one layer to the other, one should expect for each layer a temporal evolution of its normalized dark-field contrast signal similar to that of the respective reference specimen, since similar boundary conditions were applied. In fact, the top M2 layer was subjected to evaporative drying through its top surface, while the bottom M1 layer was sort of "sealed" by the presence of the other layer on top of it, thus, in principle, not directly and immediately subjected to evaporative drying. Figure 3 shows, however, an increase in normalized dark-field contrast signal for both layers of the model system.

The M1 bottom layer underwent a relative change of about 32% between the beginning and the end of the campaign, while the M2 top layer showed a corresponding relative change of about 44%. Compared with the M2 reference specimen, whose $\tilde{S}(t)$ increased of 62% within the same time interval, the top layer in the model system exhibited a smaller and slower increase, achieving a plateau value at about 5 hours against the 3 hours of the corresponding M2 reference specimen.

These two results are in agreement with the hypothesis of a displacement of water, during cement hydration, from the M1, bottom layer, to the M2, top layer.

By losing water, the M1 bottom layer underwent a change of balance between the microstructure formation, which tends to decrease the (U-)SAXS strength, and the emptying of pores, which tends to increase it [67]. A change of balance occurred also for the pore-scale processes driving the water redistribution inside the M2 top layer: the emptying of pores from water happened more slowly as a consequence of their refilling with water displaced from the bottom M1 layer.

Such water displacements are hypothesized to be driven by capillary force gradients due to the differences in local porosity and pore size distribution between the two mortar layers [1,2]. The difference in the w/c of the two layers is one of the main factors influencing the pore size distribution. Under the same boundary conditions, e.g., external temperature and RH, sealing or not, curing time, presence or absence of a curing agent and the same material components, a mortar cast with higher w/c will have coarser pores and more of such larger pores compared to the one cast at lower w/c [88].

As additional evidence of the water displacements from the M1 bottom layer to the M2 top one, we also notice that within the first 1.5 hours from casting, the normalized dark-field contrast signal increased faster for the M1 bottom layer than for the M2 top one. This fact suggests that water was pulled out from the M1 bottom layer across the interface with the M2 top layer immediately at early ages after casting the system.

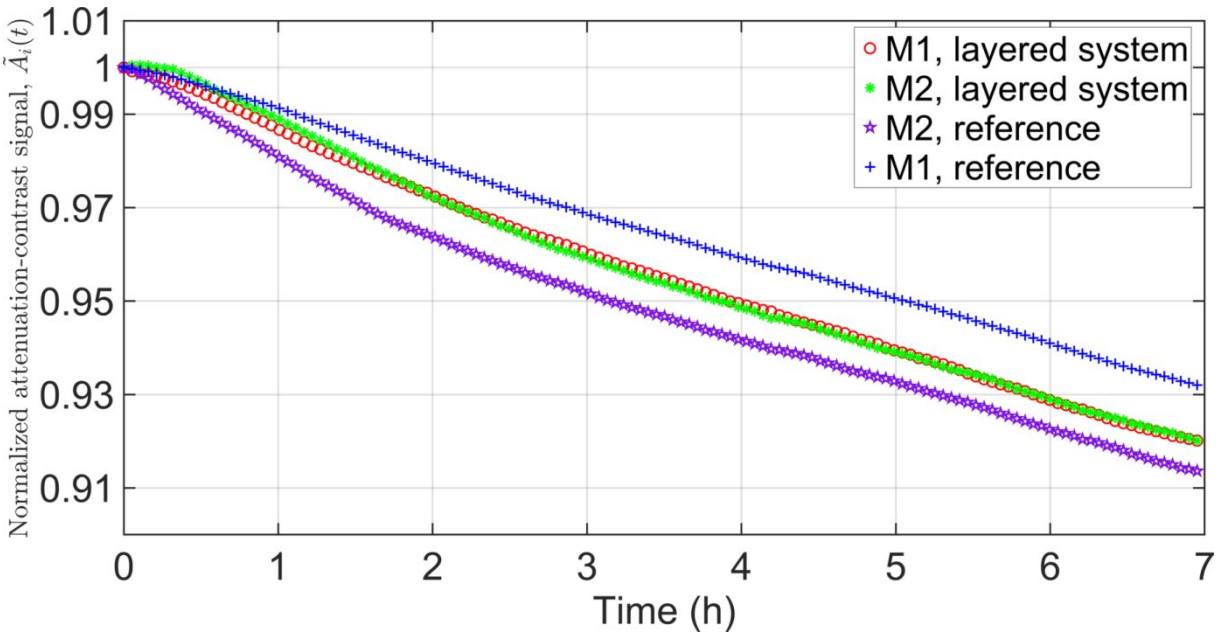

Figure 4 (with colors in the online version of the article). Temporal evolution, during the overall multi-contrast radiography campaign, of the pixel-wise average value, $A_i(t) = \langle P_\mu(x,y,t)\rangle_{(x,y)_i}$, of the linear projection P_μ of the X-ray attenuation coefficient, μ, normalized by the same average value at the beginning of the measurement campaign, $A_i(t_0)$ ($t_0 = 0$ hours). Such average values are also called normalized attenuation contrast signals and are indicated as $\tilde{A}_i(t)$, where the integer index i just enumerates them. Different curves refer to distinct regions of interest (ROIs), highlighted as rectangles in Figures 2(a)-(c) and covering the different specimens or parts thereof: M1, bottom layer in the model system (red circles); M2, top layer in the model system (green asterisk); M2 reference specimen (purple pentagram); M1 reference specimen (blue plus sign).

Figure 4 shows the evolution of the normalized attenuation contrast signal $\tilde{A}_i(t)$ for the same ROIs for which the normalized dark-field contrast one is plotted in Figure 3.

For any specimen and layer in the model layered one, $\tilde{A}_i(t)$ monotonically decreased with time. The largest relative change in $\tilde{A}_i(t)$, between the beginning and the end of the measurement campaign was achieved by the M2 reference specimen and was of about 9% while the smallest change was achieved by the M1 reference specimen and was of about 7%. These overall relative changes were, in absolute value, always much smaller than the corresponding ones for the normalized dark-field contrast signals (except for the M1 reference specimen, compare with Figure 3).

Since $\tilde{A}_i(t)$ is directly proportional to the cumulative value of μ along each ray connecting the X-ray source and a pixel position on the detector, averaged over each ROI, and given the linear dependence of μ from the mass density and from a power of the atomic number Z, any change in $\tilde{A}_i(t)$ with time is either a proxy of change in mass density or a change in chemical species. Because of the level of spatial resolution in our radiographs obtained by TLI (105 μm) and given the nature of the radiography values, i.e., cumulative values over the full, constant thickness (thus constant volume, at the length scale of the spatial resolution) of the specimen, any change in $\tilde{A}_i(t)$ can only relate to overall mass changes along each ray and for that thickness. That is because cement hydration and evaporative drying do not lead to any change in the largest possible value of Z into the material, while drying can only lead to mass changes due to water displacement and evaporation. Local changes of mass density due to cement hydration and capillary forces due to drying are likely occurring at a much smaller length scale than the specimen thickness and are randomly distributed sufficiently enough to be averaged to 0 over the specimen thickness, in addition to likely be enough small not to influence significantly the detectable changes in μ.

This interpretation of the monotonic decrease in the $\tilde{A}_i(t)$ signals agrees with the measured mass loss measured for each specimen (see Table 2): the M2 reference specimen underwent the largest mass loss as well as the largest total change in normalized attenuation contrast signal, while the M1 reference specimen underwent the smallest changes for both variables.

The interpretation here provided also agrees with the original results by Bentz et al. for drying cement pastes [1,2].

We attribute part of the mass loss of the M1 reference specimen to imperfect sealing of that specimen and part of it, as for any other specimen, to the removal of the grease deposited on the lid when closing the mold of the specimen. The hypothesis of imperfect sealing is also coherent with the observed decrease for the $\tilde{A}_i(t)$ signal of such specimen.

The smaller relative changes of the $\tilde{A}_i(t)$ signals compared with the $\tilde{S}_i(t)$ ones also validate what already reported by Yang et al. [67] and by Prade et al. [65,66] about the smaller sensitivity of X-ray attenuation contrast imaging to local water content changes during hydration and drying in cement-based materials, when compared with that of X-ray dark-field contrast imaging.

We finally observed as within the first 1.5 hours since the beginning of the experiment, the normalized attenuation contrast signal decreased slightly faster for the M1 bottom layer than for the M2 top layer, indicating faster water loss than what happening because of evaporative drying in the top layer. This fact is a further evidence of the water displacement across the interface between the two layers, from the bottom to the top, caused by the gradients in capillary forces.

Coming back to the dark-field contrast, in terms of spatial distribution P_ε looks like to have increased/decreased in a rather random fashion. An exception is the layered system, where one can observe the appearance of two regions, located at approximately 5 and 7 mm, respectively, from the specimen's top surface. These two regions are characterized by larger increases compared with the surrounding regions.

In order to obtain more details of the spatial-temporal distribution of P_ε, especially along the vertical direction of each specimen, we examined for each of them other narrow ROIs, with horizontal (X-axis) width of 5 pixels and centered in the specimens center. $P_\varepsilon(x, y, t)$ was spatially averaged over the 5 pixels of such ROIs along the X-axis, for each Y position, in order to obtain a spatial profile along the Y-axis at each time instant, $\hat{P}_j(y, t) = \langle P_\varepsilon(x, y, t)\rangle_{x,j}$, where the index j identifies such a ROI for a specimen and $\langle \dots \rangle_{x,j}$ indicates the spatial averaging over the 5 horizontal pixels for each ROI. We chose to average P_ε over such narrow and central ROI in order to capture its vertical profile, along the Y-axis of the specimen, by including also an example of the influence of the local spatial heterogeneity of the two layers not only along that direction but also along the horizontal, X-axis. Even though we are mainly interested in reporting and describing the spatial-temporal evolution of P_ε along the vertical direction of the specimen, especially across the interface region between the two layers, the overall spatial heterogeneity of the microstructure plays a role in the creation of the capillary force gradients responsible for the water displacements from the bottom to the top layer.

Figure 5 shows, for the model layered specimen (inset (a)) and for the M2 reference one (inset (b)), $\tilde{\hat{P}}_j(y, t_k)$ for five distinct time instants t_k, where $\tilde{\hat{P}}_j(y, t_k) \equiv \frac{\hat{P}_j(y,t_k)}{\hat{P}_j(y,t_0)}$ is the normalized average value at the beginning of the campaign, t_0. A similar plot but for the M1 reference specimen is reported in Section S2 of the Supplementary Materials [99].

Figure 5(a) shows that, within the first 95 minutes since the beginning of the campaign, the normalized scattering signal increased nearly at each vertical position in the layered system, except within the first 0.4 mm from the top, where it underwent a drop. The reason for this drop could be a water re-saturation during the acquisition, as the pores here may have partially dried without sealing already at the beginning of the campaign. Another possible explanation for this phenomenon is gravitational settlement of the fresh mortar, which may have been particularly evident near the top of the sample. As evaporative drying proceeded, the normalized dark-field contrast signal continued increasing within the first 4-5 hours. However, this

increase was not uniform along the vertical direction, with many regions characterized by almost no increase at all. Figure 5(b), on the contrary, shows a rather spatially homogeneous and slow increase, if any, in the normalized dark-field contrast signal, from 95 minutes on, suggesting that most of the significant increase happened already before.

The spatial homogeneous distribution in increase of (U-)SAXS "strength" suggests that the water loss due to drying occurred very rapidly, especially in the M2 reference specimen, and was rather homogeneous. No localized drying front, gradually moving from the top evaporative surface down into the specimens was observed. This is in agreement with the observations by Bentz al. in their X-ray attenuation study [1,2].

Two important results are derived from the comparison of Figures 5(a) and 5(b).

First, the layered specimen was less homogenous in the vertical direction in respect to the increase of the (U-)SAXS "strength", compared with the M2 reference specimen. This is evinced by observing the existence of two vertical positions, at approximately 5 and 7 mm from the top evaporation surface, respectively, within the layered system where the dark-field contrast signal continuously increased with time even after 95 minutes from the start of the campaign, contrary to what happened for the M2 reference specimen. Since these regions are far away from the top evaporation surface, we attribute the continuous increase in local dark-field contrast signal to a local water loss driven by highly localized capillary force gradients having larger magnitude than those in the rest of that layered specimens and larger than those in the M2 reference specimen.

Such larger capillary force gradients are assumed to have been mainly due to differences in the local porosity and pore size distribution rather than due to the creation of water-air menisci by evaporative drying. They must have also been mainly directed from the bottom of the specimen toward the top, as expected by the order of casting for the two mortars with different w/c, otherwise the high and continuous scattering growth region at about 7 mm depth from the evaporation surface should not be expected.

A detailed explanation of why these two regions in the layered specimen exhibited uninterrupted growth in (U-)SAXS "strength" because of water loss is proposed in the following section based upon the comparison with the analysis of the features of the local pore space, such that the coupling between the water displacement and the local pore structure is characterized.

We remark that such features of the local pore space spanned a length scale range including also larger values than those at which the dark-field contrast is generated. However, we hypothesize that they induced local water content changes also at smaller length scales, thus more strongly affecting the temporal evolution of the dark-field contrast signal.

The second important result inferred from the comparison between Figures 5(a) and 5(b) regards the difference in temporal scale and value of the dark-field contrast signal increase. The M2 reference specimen exhibited much faster, large and homogeneously distributed dark-field contrast increase than the M2 layer of the layered specimen (approximately the first 4 to 5

mm from the evaporation surface), in agreement with the results shown in Figure 3. This difference provides another confirmation of the displacement of water from the M1 layer to the M2 one, contributing to re-filling some of the pores of the latter, quickly and homogeneously emptied by evaporation as it occurred for the M2 reference specimen.

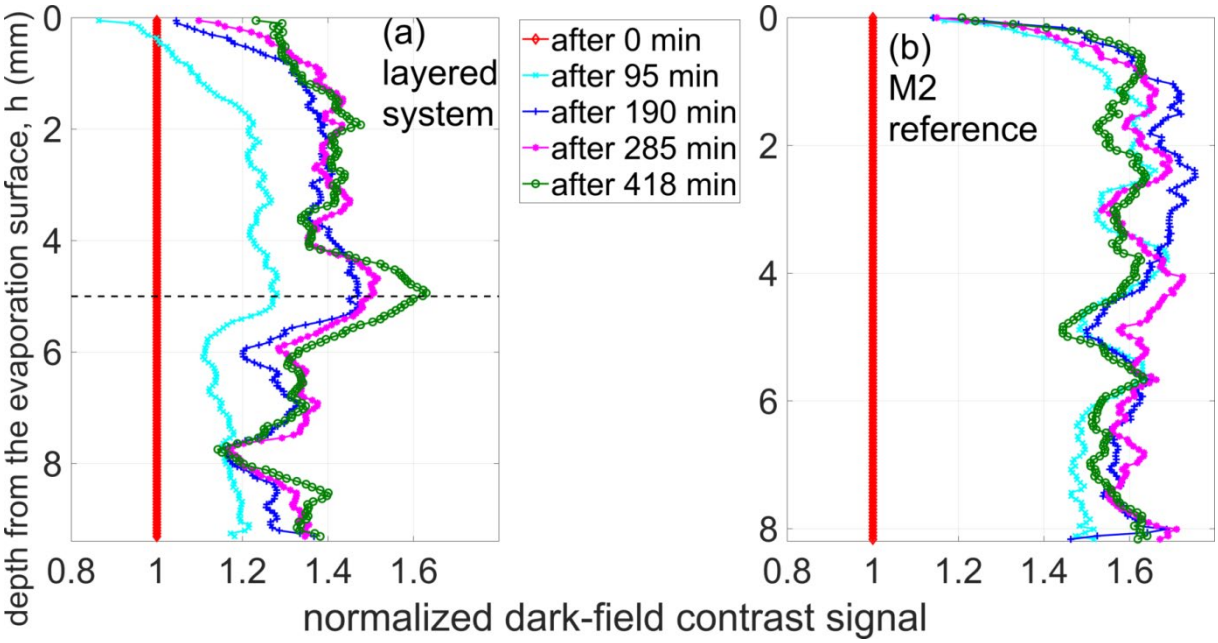

Figure 5 (with colors in the online version of the article). Normalized dark-field contrast signal profile along the Y (vertical) direction of the specimen (see Fig. 1 for the coordinate system), obtained by averaging along the X-axis of the specimen $P_\epsilon(x, y, t)$, for each Y position, in a central region 5-pixel wide, then normalizing it by the same average value at the beginning of the campaign ($t = t_0 = 0$ hours). (a): model layered system. (b): M2 reference specimen. Different curves, with distinct markers, refer to different time instants from the start of the measurement: at 0 minutes (red diamond), after 95 minutes (cyan cross), after 190 minutes (blue plus sign), after 285 minute (pink asterisk), after 418 minutes (green circle). The black, dashed, horizontal line in inset (a) indicates the approximate position of the interface between the two layers as expected from the casting and as approximately visible in the standard X-ray tomogram.

3.3. Correlation between the water transport and the pore space heterogeneity

We performed X-ray attenuation-contrast micro-tomography on the model layered system weeks after the multi-contrast X-ray radiography campaign. By 3D image analysis procedures, described in Section S4 of the Supplementary Materials [99], we segmented the part of the pore space, excluding air voids, above the spatial resolution of the tomogram, i.e., pores with size larger than 14 μm. We used the segmentation results and their quantitative analysis, in terms of pore size distribution and spatial distribution of the local porosity, for (1) qualitatively locating and distinguishing between the M1 region and the M2 region, since we knew only approximately the depth at which we should expect one mortar layer to end and the other to start, and (2) interpreting the water transport results inferred by the analysis of the dark-field contrast radiographs in terms of the local properties of such part of the pore space.

One vertical cross-section (X-Y slice) from the tomogram is shown in Figure 6(a). The blue (color in the online version of the article) rectangular region highlights the location, on that slice, of a parallelepiped ROI (582 × 724 × 1430 voxels, in X-, Y- and Z-directions, respectively). We considered only that ROI for performing the quantitative analysis of the segmented pore space. Such ROI excludes the parts of the specimen close to the boundaries, where the segmented pore space contains features, e.g., cracks, due to shrinkage.

Figure 6(a) shows representatively and qualitatively that the specimen had larger porosity (considering only the pores larger than 14 μm) and slightly larger aggregate volume fraction towards its bottom than closer to its top. The larger aggregate volume fraction is expected considering the effects of sedimentation due to gravity.

In order to set these statements more on a quantitative basis, we plotted the cumulative spatial distribution on the X-Y plane of the segmented pore space, shown in Figure 6(b). Such plot refers only to the 3D ROI whose one X-Y cross section is shown by the blue rectangle in Fig. 6(a) and it was obtained by computing the Maximum Intensity Projection of the segmented pore space along the Z-axis. The Maximum Intensity Projection image was derived by summing up all the 2D vertical cross-sections of the segmented pore space's 3D binary image. Therefore, the value of each pixel in the Maximum Intensity Projection image represents the cumulative number of voxels, classified as pore voxels, along a ray parallel to the Z-axis. For a better visualization, we rescaled the original Maximum Intensity Projection image to the 8-bit integer dynamic range [0; 255] and reset the pixel value range between the average and maximum pixel values. We chose to report the Maximum Intensity Projection image to provide a comprehensive overview of the pore distribution, especially along the vertical (Y-) direction.

A high concentration of pores is clearly visible at a vertical position about 4.5 - 5.7 mm, as shown in the yellow (color in the online version of the article) rectangle in Figure 6(b). Several large and irregularly shaped pores are visible. These pores seem to be highly interconnected, forming several local pore clusters with large size, a result confirmed by the local porosity spatial distribution analysis described in Section S4, Figure S6, of the Supplementary Materials [99]. This highly porous and interconnected region corresponds to the same region that exhibits the largest values and respective changes in the normalized dark-field contrast signal vertical profiles, at any time instant, shown in Figure 5(a). It is thus corresponding to the bright region located at approximately the same Y-position in the dark field radiographs (see Figures 2(a) to (c) and the complete time series of such radiographs provided as a movie in the Supplementary Materials [99], Section S5). In addition, we notice that the position of this region agrees with the expectations for the location of the interface between the two mortar layers.

Despite some large and almost spherical air voids, not successfully removed by the procedures for the pore space segmentation and distributed more within the top M2 layer (see the

arrows in Figure 6(b)), one can clearly observe a higher local porosity and more pores with larger size in the bottom M1 mortar than in the top M2 one. The main reason for not considering large air voids in the analysis of the pore space heterogeneity is that they play a minor role in creating the capillary force gradients during evaporative drying when compared with the other types of pores, even though they are still involved in the drying process itself (they are obstacles to the liquid water displaced during the constant rate period of the drying and water vapor can re-condensate on some regions of their inner surface while liquid water can evaporate from other such regions). The quantitative analysis of the porosity distribution along the X-axis, reported in Section S4 of the Supplementary Materials [99], corroborates this observation.

Thus, the 3D image analysis of the segmented pore space allowed us clearly identifying the most likely locations of the two mortars and the position of their interface, which was characterized by large local porosity values. We can thus establish a clear correlation between the source of large dark-field contrast pixel values, observed at the position of the interface, to both the local higher spatial heterogeneity of the specimen and, more important, to the consequent higher transport, i.e., loss, of water in that region, since it is surrounded, along the vertical axis, by regions with lower local porosity and with less irregular pores.

The interface between the two mortars may have acted as a sort of local reservoir from which water was continuously pulled out by regions above and below it, with lower local porosity. Such emptying was likely more prolonged than that occurring in the bulk of the layers or in the M2 reference specimen, thus leading to more prolonged and larger creation of new interfacial area with the maximum possible scattering contrast $|\Delta\rho_e|$ between the solid phases and air. The region above the interface, within the M2 layer, had not only lower local porosity, in comparison with the region below the interface and within the M1 layer (see Figure S6 of the Supplementary Materials [99]), but it also had on average smaller pores, as visualized by the Maximum Intensity Projection image in Figure 6(b). For these reasons, a net displacement of water from the latter to the former could take place, leading to a gradual drying of the bottom M1 layer. This was already hypothesized before, based upon the increase in its dark-field contrast signal instead of a decrease, normally occurring in the absence of drying for the same type of mortar (Figures 2(a) to (c)).

Additional support to the conclusion that water was continuously drawn from the M1 layer towards the M2 layer, through their interface region, comes from observing that a region with larger local porosity than in its top surroundings is located in M1 at about 7 mm depth from the top evaporation surface (see Fig. 6(b), cyan rectangle). This region extends across the full horizontal (X-direction) length of the specimen. It corresponds, along the vertical direction, to the region where the second peak in the vertical profile of the normalized dark-field contrast signal is located (Figure 5(a)). It contains highly interconnected coarse porous patches, similar to the ones observed at the interface between M1 and M2. These patches may also have acted as buffers of water drawn by the capillary force gradients towards the M2 layer. The presence

of more irregular and coarser porous patches in the cement matrix of M1, compared with M2, is in agreement with the observation of a slightly larger volume fraction of aggregates in the bottom M1 layer than in the top M2 layer.

As already observed by Diamond [89], porous patches tend to be highly interconnected with each other, thus likely contributing to increasing the liquid diffusivity and permeability of mortar and concrete. The latter conclusion agrees with the dark-field contrast radiography results, with consequent support of the interpretation of the changes in the dark-field contrast signals.

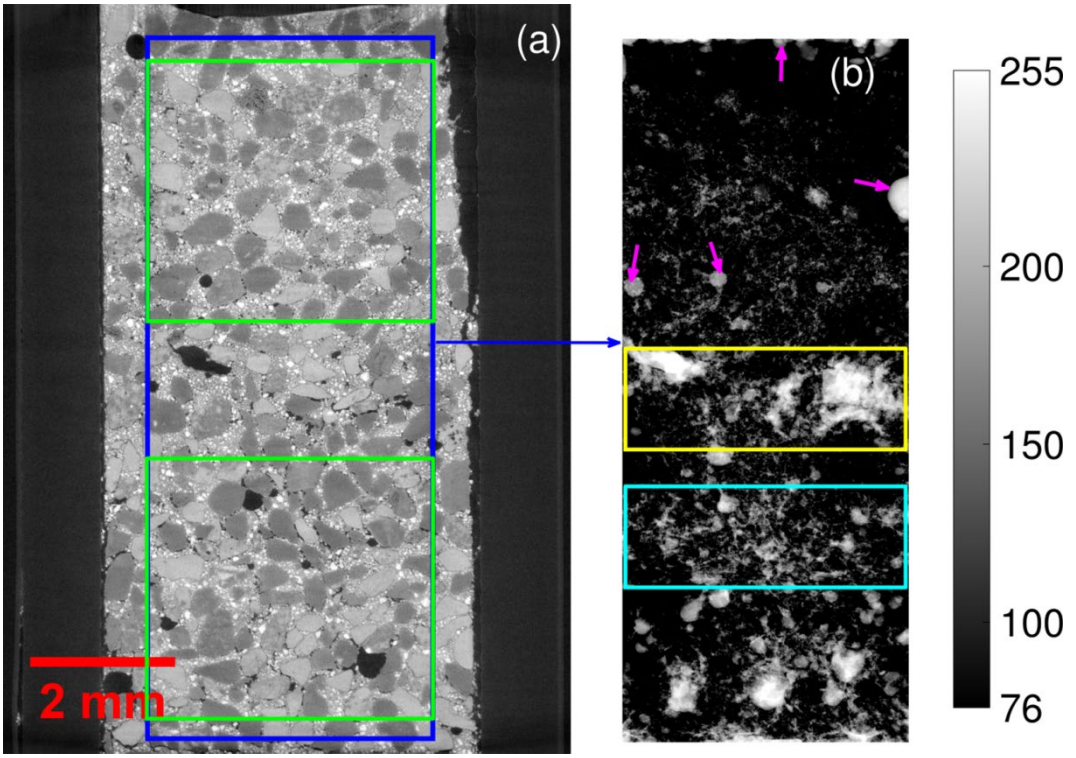

Figure 6 (with colors in the online version of the article). (a) Vertical (X-Y) cross-section from the conventional high resolution attenuation contrast micro-tomography image of the model layered system. The blue rectangle shows the position, on that cross-section, of a 3D, parallelepiped ROI within which the pore space was segmented and analyzed (see Section S4 of the Supplementary Materials [99]). (b) Maximum Intensity Projection of all the vertical cross-sections of the 3D binary image of the segmented pore space, considering only the ROI highlighted on a single cross-section by the blue rectangle in inset (a). The green rectangles in inset (a) indicate the locations, on that cross-section, of two other parallelepiped ROIs inside the top M2 layer and in the bottom M1 layer. The yellow and cyan rectangles in inset (b) highlight the projection on the X-Y plane of two highly porous regions where the two main peaks observed in the vertical profiles of the normalized scattering signal were observed at any time instant (Figure 5). The arrows inside the Maximum Intensity Projection image in inset (b) point to some air voids not successfully excluded from the pore space 3D binary image.

While Figure 6(b) provides only qualitative evidence about differences in local porosity and pore size distribution in the regions of the two mortars and within their interfacial region, Figure 7 reports quantitative data in the form of cumulative porosity as a function of the pore "diameter" obtained from the continuous pore size distribution of the 3D binary image of the

segmented pore space. The analysis was performed independently for two parallelepiped ROIs contained within the M1 and M2 regions of the model layered system (one vertical (X-Y) cross-section of each ROI is shown by the top and bottom green rectangles in Figure 6(a)).

The ROI within the M1 layer exhibited both higher total porosity (about 1.5%, down to a pore size lower bound equal to the approximate spatial resolution of the tomogram, i.e., 14 μm) and a larger fraction of pore volume with larger radius (range of 50 to 100 μm) compared with the ROI within the M2 layer (about 0.7% total porosity). The existence of slightly larger cumulative porosity in correspondence of the largest values of pore diameter, from about 220 μm on, within the M2 ROI is in contradiction with what expected and with what observed for the rest of the pore size range. This is possibly an artifact due to the unsuccessful complete exclusion of large air voids from the 3D binary image of the segmented pore space at the top of the M2 layer.

We note again that the estimates of the total porosity for the two ROIs within the two respective mortar layers are based only upon pores with size larger than the spatial resolution of the tomogram, i.e., 14 μm, and after excluding the large air voids.

3.4. Increased sensitivity in detecting water transport by X-ray dark-field imaging

The previous work by Bentz et al. consisted of spatially mapping in 1D the temporal changes in X-ray transmission during hydration of a similar model layered system made of cement pastes instead of mortar as done in this work. That work already showed the possibility of detecting water displacement from paste layers with higher w/c to paste layers with lower w/c [1,2].

Compared with our study, Bentz et al. achieved much lower spatial and temporal resolutions, given the type of X-ray attenuation-contrast instrument available at the time of their work. Despite they performed point-wise X-ray transmission measurements along a vertical line, with a step of 200 μm, the actual spatial resolution was smaller, due to the size of the illuminating beam and of the pinhole in front of the point-like detector (1 mm for both) [2]. Since the measurements were point-wise, with the need of moving the specimen relatively to the source and detector position, the transmission values at different vertical locations were not simultaneous, even though the measurement at a single point was much faster (5 s [2]) than the time required for a single phase-stepping protocol in our TLI measurements (191 s).

An improvement of the original setup used by Bentz et al. was obtained by using a 2D detector, which allowed achieving higher spatial resolution (80 μm pixel size [35], thus likely 160 μm effective spatial resolution, for a FOV covering a specimen size of the same order of magnitude of that used in our study).

Our approach, based upon X-ray dark-field contrast, is characterized by a relevant improvement compared with what achieved so far by X-ray attenuation contrast measurements. Such

improvement concerns the signal changes due to the water transport process in systems with similar ranges of pore sizes.

In our study, the relative difference in the maximum dark-field contrast signal temporal change between the top M2 layer of the model layered system and the corresponding M2 reference specimen, both subjected to drying, was about -30%. Such difference was due to the supply of water to the M2 layer by the M1 one, supply which did not occur in the reference M2 specimen.

The same type of difference between the bottom M1 layer and the corresponding M1 reference specimen was about 112%, due to the loss of water occurring in the M1 layer but not in the M1 reference mortar.

Since Bentz et al. performed their X-ray transmission measurements on one similar layered system (0.30 w/c layer on top of a 0.45 w/c) and respective reference specimens, with the exception of investigating only cement pastes, it was possible to perform similar calculations of relative differences in maximum X-ray transmission signal changes inside the two cement paste types. For the 0.3 w/c paste the difference was about 4% while for the 0.45 one it was about 7%, calculated at 8 hours after the initial setting time. Thus X-ray dark-field contrast imaging shows to be much more sensitive to changes in local water content [65–67] due to water displacements driven by capillary force gradients created by both cement hydration and evaporative drying.

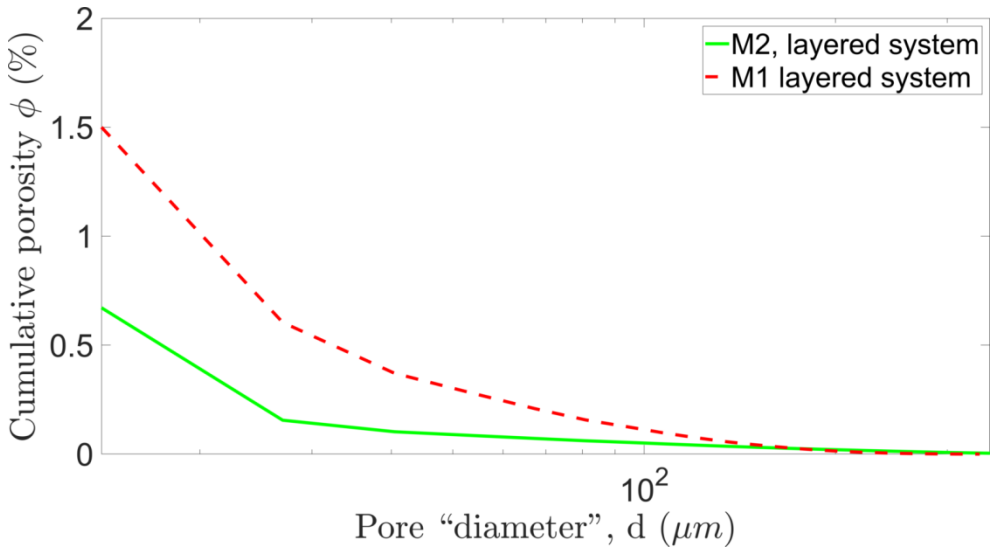

Figure 7 (with colors in the online version of the article). Cumulative porosity ϕ as a function of the pore "diameter" d, obtained by the continuous pore size distribution analysis proposed by Münch & Holzer [90] and applied to the 3D binary image of the segmented pore space, derived by 3D image analysis of the tomogram of the model layered system. The solid line refers to the 3D region of interest of the tomogram highlighted by the top green parallelepiped (rectangle in that cross-section) in Figure 6(a), contained within the M2 top layer. The dashed line refers to the 3D region of interest of the same tomogram highlighted by the bottom green parallelepiped one vertical cross-section of which is also shown in Figure 6(a), contained within the M1 bottom layer. $\phi(d)$ represents the amount of segmented pore volume (normalized by the region of interest's total volume)

coverable by spheres of diameter larger than d. The range of pore diameter d on the horizontal axis has a lower bound equal to the approximate estimate of the spatial resolution in the tomogram, i.e., 14 μm.

4. Conclusions and outlook

We present in this article the results of an experimental campaign aiming at imaging the two-dimensional spatial-temporal distribution of water in a two-layer mortar system within the first 7 hours since casting. The two layers were cast with different water-to-cement ratios, to create regions with different pore size distributions. The specimen was subject to evaporative drying only through its top surface. The layer with lower water-to-cement ratio value was cast on top of the one with higher water-to-cement ratio.

The imaging approach we exploited was based upon multi-contrast X-ray radiography obtained via Talbot-Lau interferometry with a laboratory-scale instrument. Such approach allowed us obtaining not only a time series of standard, attenuation-based X-ray radiographs, which have much more limited sensitivity to local changes in pore-scale water content but also a simultaneous time series of dark-field X-ray radiographs, which, as shown here and in previous work [65–67], are much more sensitive to those local changes.

Finally, we used standard attenuation contrast X-ray micro-tomography, performed after the multi-contrast X-ray radiography campaign, to quantitatively characterize the part of the pore space with a size above a certain length scale (14 μm, the spatial resolution of the tomogram) and its spatial heterogeneity.

Beyond observing (with higher spatial, temporal and water content resolutions) qualitatively a similar behavior for the local water content changes as observed by Bentz et al. by standard X-ray attenuation contrast imaging, the combination of the X-ray dark-field contrast radiography with the pore space analysis by X-ray attenuation contrast micro-tomography has allowed us to validate the hypothesis proposed by Bentz et al. for explaining the drying mechanisms of the higher water-to-cement ratio layer. The drying of the bottom layer does not in fact occur due to evaporative drying driven by air invasion percolation from the external environment, but due to the capillary force gradients directed towards the top, lower water-to-cement ratio layer, which tend to displace water from the larger pores in the bottom layer to the smaller pores in the top layer.

The relevance of such result is two-fold: on the one side, the role played by the spatial heterogeneity in the pore size distribution and local porosity in determining early-age water displacements in cement-based materials is confirmed; on the other side, the correlation between X-ray dark-field contrast signal changes and local, pore-scale water content changes is further validated.

The latter feature of our results shows the potential of X-ray dark-field contrast imaging to become a complementary method to other imaging methods (e.g., neutron or magnetic resonance imaging) in investigating water transport in early-age cement-based materials, whose

better understanding stands at the basis of improving internal curing methods and designing cement-based repair materials for already cast concrete structures.

Improvements in the understanding of the physical formation of the X-ray dark-field contrast images and in the Talbot-Lau interferometry method are still necessary to provide a more robust and complete understanding of the couplings between water transport and features of the pore structure at early ages.

On the one hand, further theoretical and experimental characterization of the correlation between the dark-field contrast signal and the pore structure could lead to more quantitative information about the coupled microstructure evolution and the water transport at the pore scale. So far, a complete framework and methodological approach to obtain quantitative information about the pore space and the local water saturation degree is not yet available. What has been proposed is only a framework relating the dark-field contrast signal to the particle size distribution and local volumetric fraction of model systems of particles, e.g., colloidal suspensions [62–64,91].

Performing the Talbot-Lau interferometry and single point ultra-small angle X-ray or neutron scattering measurements on the same exact specimens during repeated drying (or other types of liquid transport) experiments, for example with hardened cement pastes and mortars, would support the establishment of such correlation. Ultra-small angle experiments offer the advantage of distinguishing the contribution to scattering by features and processes at distinct length scales. Thus they could provide more evidence about the distinct contributions of water loss and gain to the pore-scale mechanisms inducing changes in the dark-field contrast signals and the respective length scales at which the different mechanisms mainly occur. The execution of ultra-small (and not only small) angle scattering measurements would also allow covering a range of length scales with an upper bound overlapping with the range of the best spatial resolution achievable with X-ray dark-field contrast imaging setups, especially those exploiting synchrotron radiation.

On the other hand, advances in fabrication of the gratings, e.g., the production of gratings with larger surface area [92] and/or the realization of gratings working at higher design energies [93], will allow imaging larger specimens without significant decrease in spatial resolution, compared with the resolution achieved in this work. New approaches to performing Talbot-Lau interferometry [94–97] at different specimen orientations, combined with iterative tomographic reconstruction algorithms [98], will also allow in the next years increasing the temporal resolution of 3D, tomographic imaging such that it will become possible to investigate water transport in early-age cement-based materials fully (and more quantitatively) in 3D.

Acknowledgments

We acknowledge the financial support by the Swiss National Science Foundation via projects n°143782 and n°162572, by the Helmholtz Virtual Institute for New X-ray analytical Methods in Materials science (VI-NXMM, http://roentgenbildgebung.de), and the DFG Gottfried Wilhelm Leibniz program. This work was carried out with the support of the Karlsruhe Nano Micro Facility (www.kit.edu/knmf), a Helmholtz Research Infrastructure at Karlsruhe Institute of Technology. We thank Pascal Meyer and Jürgen Mohr, Institute of Microstructure Technology at the Karlsruhe Institute of Technology, for the supply of the gratings of the Talbot-Lau interferometer at the XXXXXX, within the framework of the VI-NXMM. We would like to thank also Boris Ingold, XXX at XXX, for the help with the specimen preparation. Finally, F. P. acknowledges Dr. Klaus Achterhold for his technical and administrative support during writing of this manuscript.

We finally would like to thank the anonymous reviewer for his/her useful comments and suggestions about comparing the results of our dark-field contrast imaging measurements with SAXS and SANS measurement results already reported in the literature and related with hydrating cement paste both in the absence and in the presence of evaporative drying.

References

[1] D.P. Bentz, K.K. Hansen, H.D. Madsen, F. Vallee, E. Griesel, Drying / hydration in cement pastes during curing, Mater. Struct. 34 (2001) 557–565.

[2] D.P. Bentz, K.K. Hansen, Preliminary observations of water movement in cement pastes during curing using X-ray absorption, Cem. Concr. Res. 30 (2000) 1157–1168. doi:10.1016/S0008-8846(00)00273-8.

[3] Z. Zhang, M. Thiery, V. Baroghel-Bouny, M.D. Nguyen, P. Rossi, Modelling of the hydration and moisture transfer coupling effects on the microstructure properties of the concrete cover, in: 2nd Int. Conf. Microstruct.-Relat. Durab. Cem. Compos., RILEM Publications SARL, Amsterdam, The Netherlands, 2013: pp. 960–968.

[4] F.R. and J.W. P.Lura, B. Pease, Guy Mazzotta, Influence of Shrinkage-Reducing Admixtures on Development of Plastic Shrinkage Cracks, ACI Mater. J. 104 (2007) 187–194. doi:10.14359/18582.

[5] G.W. Scherer, Drying, Shrinkage, and Cracking of Cementitious Materials, Transp. Porous Media. 110 (2015) 311–331. doi:10.1007/s11242-015-0518-5.

[6] O.M. Jensen, P.F. Hansen, Water-entrained cement-based materials: II. Experimental observations, Cem. Concr. Res. 32 (2002) 973–978.

[7] O.M. Jensen, P.F. Hansen, Water-entrained cement-based materials: I. Principles and theoretical background, Cem. Concr. Res. 31 (2001) 647–654.

[8] O.M. Jensen, P. Lura, Techniques and materials for internal water curing of concrete, Mater. Struct. 39 (2006) 817–825. doi:10.1617/s11527-006-9136-6.

[9] L. Courard, J.-F. Lenaers, F. Michel, A. Garbacz, Saturation level of the superficial zone of concrete and adhesion of repair systems, Constr. Build. Mater. 25 (2011) 2488–2494. doi:10.1016/j.conbuildmat.2010.11.076.

[10] J. Zhou, G. Ye, K. van Breugel, Cement hydration and microstructure in concrete repairs with cementitious repair materials, Constr. Build. Mater. 112 (2016) 765–772. doi:10.1016/j.conbuildmat.2016.02.203.

[11] D.P. Bentz, K.A. Snyder, Protected paste volume in concrete: extension to internal curing using saturated lightweight fine aggregate, Cem. Concr. Res. 29 (1999) 1863–1867.

[12] P. Lura, D.P. Bentz, D.A. Lange, K. Kovler, A. Bentur, K. van Breugel, Measurement of water transport from saturated pumice aggregates to hardening cement paste, Mater. Struct. 39 (2006) 861–868. doi:10.1617/s11527-006-9137-5.

[13] P. Lehmann, S. Assouline, D. Or, Characteristic lengths affecting evaporative drying of porous media, Phys. Rev. E. 77 (2008). doi:10.1103/PhysRevE.77.056309.

[14] D. Or, P. Lehmann, E. Shahraeeni, N. Shokri, Advances in Soil Evaporation Physics—A Review, Vadose Zone J. 12 (2013) 0. doi:10.2136/vzj2012.0163.

[15] P. Zhang, F.H. Wittmann, P. Lura, H.S. Müller, S. Han, T. Zhao, Application of neutron imaging to investigate fundamental aspects of durability of cement-based materials: A review, Cem. Concr. Res. 108 (2018) 152–166. doi:10.1016/j.cemconres.2018.03.003.

[16] I. Maruyama, M. Kanematsu, T. Noguchi, H. Iikura, A. Teramoto, H. Hayano, Evaluation of water transfer from saturated lightweight aggregate to cement paste matrix by neutron radiography, Nucl. Instrum. Methods Phys. Res. Sect. Accel. Spectrometers Detect. Assoc. Equip. 605 (2009) 159–162. doi:10.1016/j.nima.2009.01.138.

[17] P. Trtik, B. Münch, W.J. Weiss, A. Kaestner, I. Jerjen, L. Josic, E. Lehmann, P. Lura, Release of internal curing water from lightweight aggregates in cement paste investigated by neutron and X-ray tomography, Nucl. Instrum. Methods Phys. Res. Sect. Accel. Spectrometers Detect. Assoc. Equip. 651 (2011) 244–249. doi:10.1016/j.nima.2011.02.012.

[18] P. Lura, M. Wyrzykowski, C. Tang, E. Lehmann, Internal curing with lightweight aggregate produced from biomass-derived waste, Cem. Concr. Res. 59 (2014) 24–33. doi:10.1016/j.cemconres.2014.01.025.

[19] C. Schroefl, V. Mechtcherine, P. Vontobel, J. Hovind, E. Lehmann, Sorption kinetics of superabsorbent polymers (SAPs) in fresh Portland cement-based pastes visualized and quantified by neutron radiography and correlated to the progress of cement hydration, Cem. Concr. Res. 75 (2015) 1–13. doi:10.1016/j.cemconres.2015.05.001.

[20] P. Trtik, B. Muench, W.J. Weiss, G. Herth, A. Kaestner, E. Lehmann, P. Lura, W. Brameshuber, Neutron tomography measurements of water release from superabsorbent polymers in cement paste, in: Int. RILEM Conf. Mater. Sci. Aachen Ger., 2010: pp. 6–10. http://library.eawag-empa.ch/empa_publications_2010_open_access/EMPA20100601.pdf (accessed March 18, 2015).

[21] M. Wyrzykowski, P. Trtik, B. Münch, J. Weiss, P. Vontobel, P. Lura, Plastic shrinkage of mortars with shrinkage reducing admixture and lightweight aggregates studied by neutron tomography, Cem. Concr. Res. 73 (2015) 238–245. doi:10.1016/j.cemconres.2015.03.013.

[22] E. Perfect, C.L. Cheng, M. Kang, H.Z. Bilheux, J.M. Lamanna, M.J. Gragg, D.M. Wright, Neutron imaging of hydrogen-rich fluids in geomaterials and engineered porous media: A review, Earth-Sci. Rev. 129 (2014) 120–135. doi:10.1016/j.earscirev.2013.11.012.

[23] D. Liu, D. Hussey, M.V. Gubarev, B.D. Ramsey, D. Jacobson, M. Arif, D.E. Moncton, B. Khaykovich, Demonstration of achromatic cold-neutron microscope utilizing axisymmetric focusing mirrors, Appl. Phys. Lett. 102 (2013) 183508. doi:10.1063/1.4804178.

[24] P. Trtik, J. Hovind, C. Grünzweig, A. Bollhalder, V. Thominet, C. David, A. Kaestner, E.H. Lehmann, Improving the Spatial Resolution of Neutron Imaging at Paul Scherrer Institut – The Neutron Microscope Project, Phys. Procedia. 69 (2015) 169–176. doi:10.1016/j.phpro.2015.07.024.

[25] C. Choi, B.J. Balcom, S.D. Beyea, T.W. Bremner, P.E. Grattan-Bellew, R.L. Armstrong, Spatially resolved pore-size distribution of drying concrete with magnetic resonance imaging, J. Appl. Phys. 88 (2000) 3578. doi:10.1063/1.1289217.

[26] P.F. Faure, S. Caré, J. Magat, T. Chaussadent, Drying effect on cement paste porosity at early age observed by NMR methods, Constr. Build. Mater. 29 (2012) 496–503. doi:10.1016/j.conbuildmat.2011.07.012.

[27] M. Van Landeghem, J.-B. d'Espinose de Lacaillerie, B. Blümich, J.-P. Korb, B. Bresson, The roles of hydration and evaporation during the drying of a cement paste by localized NMR, Cem. Concr. Res. 48 (2013) 86–96. doi:10.1016/j.cemconres.2013.01.012.

[28] J. Mitchell, T.C. Chandrasekera, D.J. Holland, L.F. Gladden, E.J. Fordham, Magnetic resonance imaging in laboratory petrophysical core analysis, Phys. Rep. 526 (2013) 165–225. doi:10.1016/j.physrep.2013.01.003.

[29] R.T. Armstrong, H. Ott, A. Georgiadis, M. Rücker, A. Schwing, S. Berg, Subsecond pore-scale displacement processes and relaxation dynamics in multiphase flow, Water Resour. Res. 50 (2014) 9162–9176. doi:10.1002/2014WR015858.

[30] K.J. Dobson, S.B. Coban, S. McDonald, J.N. Walsh, R.C. Atwood, P.J. Withers, 4-D imaging of subsecond dynamics in pore-scale processes using real-time synchrotron X-ray tomography, Solid Earth. 7 (2016) 1059.

[31] T. Bultreys, M.A. Boone, M.N. Boone, T. De Schryver, B. Masschaele, D. Van Loo, L. Van Hoorebeke, V. Cnudde, Real-time visualization of Haines jumps in sandstone with laboratory-based microcomputed tomography: VISUALIZING HAINES JUMPS WITH LAB-BASED MICRO-CT, Water Resour. Res. 51 (2015) 8668–8676. doi:10.1002/2015WR017502.

[32] J. Banhart, Advanced Tomographic Methods in Materials Research and Engineering., Oxford University Press, Oxford, UK, 2008.

[33] R. Flückiger, F. Marone, M. Stampanoni, A. Wokaun, F.N. Büchi, Investigation of liquid water in gas diffusion layers of polymer electrolyte fuel cells using X-ray tomographic microscopy, Electrochimica Acta. 56 (2011) 2254–2262. doi:10.1016/j.electacta.2010.12.016.

[34] R.A. Ketcham, G.J. Iturrino, Nondestructive high-resolution visualization and measurement of anisotropic effective porosity in complex lithologies using high-resolution X-ray computed tomography *, 302 (2005) 92–106. doi:10.1016/j.jhydrol.2004.06.037.

[35] R. Henkensiefken, T. Nantung, J. Weiss, Saturated Lightweight Aggregate for Internal Curing in Low w/c Mixtures: Monitoring Water Movement Using X-ray Absorption: Monitoring Water Movement From LWA Using X-ray, Strain. 47 (2011) e432–e441. doi:10.1111/j.1475-1305.2009.00626.x.

[36] M. Lukovic, G. Ye, Effect of Moisture Exchange on Interface Formation in the Repair System Studied by X-ray Absorption, Materials. 9 (2015) 2. doi:10.3390/ma9010002.

[37] G. Sant, A. Eberhardt, D. Bentz, J. Weiss, Influence of shrinkage-reducing admixtures on moisture absorption in cementitious materials at early ages, J. Mater. Civ. Eng. 22 (2010) 277–286.

[38] G. Sant, J. Weiss, Using X-ray absorption to assess moisture movement in cement-based materials, J. ASTM Int. 6 (2009) 1–15.

[39] A. Pourasee, A. Peled, J. Weiss, Fluid Transport in Cracked Fabric-Reinforced-Cement-Based Composites, J. Mater. Civ. Eng. 23 (2011) 1227–1238. doi:10.1061/(ASCE)MT.1943-5533.0000289.

[40] I.S. Darma, T. Sugiyama, M.A.B. Promentilla, Application of X-Ray CT to Study Diffusivity in Cracked Concrete Through the Observation of Tracer Transport, J. Adv. Concr. Technol. 11 (2013) 266–281.

[41] N. Shokri, M. Sahimi, Structure of drying fronts in three-dimensional porous media, Phys. Rev. E. 85 (2012). doi:10.1103/PhysRevE.85.066312.

[42] R.T. Armstrong, A. Georgiadis, H. Ott, D. Klemin, S. Berg, Critical capillary number: Desaturation studied with fast X-ray computed microtomography: MICROTOMOGRAPHY IMAGED DESATURATION, Geophys. Res. Lett. 41 (2014) 55–60. doi:10.1002/2013GL058075.

[43] S. Berg, H. Ott, S.A. Klapp, A. Schwing, R. Neiteler, N. Brussee, A. Makurat, L. Leu, F. Enzmann, J.-O. Schwarz, M. Kersten, S. Irvine, M. Stampanoni, Real-time 3D imaging of Haines jumps in porous media flow, Proc. Natl. Acad. Sci. 110 (2013) 3755–3759. doi:10.1073/pnas.1221373110.

[44] K. Brown, S. SchlüTer, A. Sheppard, D. Wildenschild, On the challenges of measuring interfacial characteristics of three-phase fluid flow with x-ray microtomography: IMAGING THREE-PHASE FLOW, J. Microsc. 253 (2014) 171–182. doi:10.1111/jmi.12106.

[45] M. Andrew, B. Bijeljic, M.J. Blunt, Pore-by-pore capillary pressure measurements using X-ray microtomography at reservoir conditions: Curvature, snap-off, and remobilization of residual CO_2, Water Resour. Res. 50 (2014) 8760–8774. doi:10.1002/2014WR015970.

[46] M. Andrew, B. Bijeljic, M.J. Blunt, Pore-scale imaging of geological carbon dioxide storage under in situ conditions: PORE-SCALE IMAGING OF CARBON STORAGE, Geophys. Res. Lett. 40 (2013) 3915–3918. doi:10.1002/grl.50771.

[47] S. Youssef, H. Deschamps, J. Dautriat, E. Rosenberg, R. Oughanem, E. Maire, R. Mokso, 4d imaging of fluid flow dynamics in natural porous media by ultra-fast xray microtomography, in: Int. Symp. SCA Napa Val. Calif., 2013. http://www.scaweb.org/assets/papers/2013_papers/SCA2013-012.pdf (accessed February 28, 2015).

[48] F. Yang, M. Griffa, A. Bonnin, R. Mokso, C. Di Bella, B. MüNch, R. Kaufmann, P. Lura, Visualization of water drying in porous materials by X-ray phase contrast imaging, J. Microsc. 261 (2016) 88–104. doi:10.1111/jmi.12319.

[49] F. Yang, M. Griffa, A. Hipp, H. Derluyn, P. Moonen, R. Kaufmann, M.N. Boone, F. Beckmann, P. Lura, Advancing the visualization of pure water transport in porous materials by fast, talbot interferometry-based multi-contrast x-ray micro-tomography, in: S.R. Stock, B. Müller, G. Wang (Eds.), 2016: p. 99670L. doi:10.1117/12.2236221.

[50] A. Bravin, Exploiting the X-ray refraction contrast with an analyser: the state of the art, J. Phys. Appl. Phys. 36 (2003) A24.

[51] T.E. Gureyev, S.C. Mayo, D.E. Myers, Y. Nesterets, D.M. Paganin, A. Pogany, A.W. Stevenson, S.W. Wilkins, Refracting Röntgen's rays: Propagation-based x-ray phase contrast for biomedical imaging, J. Appl. Phys. 105 (2009) 102005. doi:10.1063/1.3115402.

[52] R. Mokso, F. Marone, S. Irvine, M. Nyvlt, D. Schwyn, K. Mader, G.K. Taylor, H.G. Krapp, M. Skeren, M. Stampanoni, Advantages of phase retrieval for fast x-ray tomographic microscopy, J. Phys. Appl. Phys. 46 (2013) 494004. doi:10.1088/0022-3727/46/49/494004.

[53] A. Olivo, K. Ignatyev, P.R. Munro, R.D. Speller, Noninterferometric phase-contrast images obtained with incoherent x-ray sources, Appl. Opt. 50 (2011) 1765–1769.

[54] H. Wang, Y. Kashyap, K. Sawhney, From synchrotron radiation to lab source: advanced speckle-based X-ray imaging using abrasive paper, Sci. Rep. 6 (2016) 20476. doi:10.1038/srep20476.

[55] I. Zanette, T. Zhou, A. Burvall, U. Lundström, D.H. Larsson, M. Zdora, P. Thibault, F. Pfeiffer, H.M. Hertz, Speckle-Based X-Ray Phase-Contrast and Dark-Field Imaging with a Laboratory Source, Phys. Rev. Lett. 112 (2014). doi:10.1103/PhysRevLett.112.253903.

[56] F. Pfeiffer, C. Kottler, O. Bunk, C. David, Hard X-Ray Phase Tomography with Low-Brilliance Sources, Phys. Rev. Lett. 98 (2007). doi:10.1103/PhysRevLett.98.108105.

[57] F. Pfeiffer, T. Weitkamp, O. Bunk, C. David, Phase retrieval and differential phase-contrast imaging with low-brilliance X-ray sources, Nat. Phys. 2 (2006) 258–261. doi:10.1038/nphys265.

[58] M. Bech, O. Bunk, T. Donath, R. Feidenhans'l, C. David, F. Pfeiffer, Quantitative x-ray dark-field computed tomography, Phys. Med. Biol. 55 (2010) 5529–5539. doi:10.1088/0031-9155/55/18/017.

[59] P. Debye, A.M. Bueche, Scattering by an Inhomogeneous Solid, J. Appl. Phys. 20 (1949) 518. doi:10.1063/1.1698419.

[60] P. Debye, H.R. Anderson, H. Brumberger, Scattering by an Inhomogeneous Solid. II. The Correlation Function and Its Application, J. Appl. Phys. 28 (1957) 679. doi:10.1063/1.1722830.

[61] S. Torquato, Random Heterogeneous Materials, Springer New York, New York, NY, 2002. http://link.springer.com/10.1007/978-1-4757-6355-3 (accessed October 27, 2016).

[62] M. Strobl, General solution for quantitative dark-field contrast imaging with grating interferometers, Sci. Rep. 4 (2014) 7243. doi:10.1038/srep07243.

[63] F. Prade, A. Yaroshenko, J. Herzen, F. Pfeiffer, Short-range order in mesoscale systems probed by X-ray grating interferometry, Europhys. Lett. EPL. 112 (2015) 68002/1–7. doi:10.1209/0295-5075/112/68002.

[64] S. Gkoumas, P. Villanueva-Perez, Z. Wang, L. Romano, M. Abis, M. Stampanoni, A generalized quantitative interpretation of dark-field contrast for highly concentrated microsphere suspensions, Sci. Rep. 6 (2016) 35259. doi:10.1038/srep35259.

[65] F. Prade, K. Fischer, D. Heinz, P. Meyer, J. Mohr, F. Pfeiffer, Time resolved X-ray Dark-Field Tomography Revealing Water Transport in a Fresh Cement Sample, Sci. Rep. 6 (2016) 29108. doi:10.1038/srep29108.

[66] F. Prade, M. Chabior, F. Malm, C.U. Grosse, F. Pfeiffer, Observing the setting and hardening of cementitious materials by X-ray dark-field radiography, Cem. Concr. Res. 74 (2015) 19–25. doi:10.1016/j.cemconres.2015.04.003.

[67] F. Yang, F. Prade, M. Griffa, I. Jerjen, C. Di Bella, J. Herzen, A. Sarapata, F. Pfeiffer, P. Lura, Dark-field X-ray imaging of unsaturated water transport in porous materials, Appl. Phys. Lett. 105 (2014) 154105.

[68] R. Sudol, B.J. Thompson, Lau effect: theory and experiment, Appl. Opt. 20 (1981) 1107–1116.

[69] H.F. Talbot, Facts relating to Optical Science. No. IV., Lond. Edinb. Philos. Mag. J. Sci. 9 (1836) 401–407.

[70] C. David, B. Nöhammer, H.H. Solak, E. Ziegler, Differential x-ray phase contrast imaging using a shearing interferometer, Appl. Phys. Lett. 81 (2002) 3287. doi:10.1063/1.1516611.

[71] T. Weitkamp, B. Nöhammer, A. Diaz, C. David, E. Ziegler, X-ray wavefront analysis and optics characterization with a grating interferometer, Appl. Phys. Lett. 86 (2005) 054101. doi:10.1063/1.1857066.

[72] L.A. Feldkamp, L.C. Davis, J.W. Kress, Practical cone-beam algorithm, JOSA A. 1 (1984) 612–619.

[73] M. Kriechbaum, G. Degovics, J. Tritthart, P. Laggner, Fractal structure of Portland cement paste during age hardening analyzed by small-angle x-ray scattering, in: P. Bothorel, E.J. Dufourc (Eds.), Trends Colloid Interface Sci. III, Steinkopff, Darmstadt, 1989: pp. 101–105. doi:10.1007/BFb0116194.

[74] M. Kriechbaum, G. Degovics, P. Laggner, J. Tritthart, Investigations on cement pastes by small-angle X-ray scattering and BET: the relevance of fractal geometry, Adv. Cem. Res. 6 (1994) 93–101. doi:10.1680/adcr.1994.6.23.93.

[75] F. Häussler, F. Eichhorn, H. Baumbach, Description of the structural evolution of a hydrating portland cement paste by SANS, Phys. Scr. 50 (1994) 210–214. doi:10.1088/0031-8949/50/2/020.

[76] F. Häussler, M. Hempel, F. Eichhorn, A. Hempel, H. Baumbach, Hydrating cement pastes as a complex disordered system, Phys. Scr. T57 (1995) 184–189. doi:10.1088/0031-8949/1995/T57/032.

[77] A.J. Allen, J.J. Thomas, Analysis of C–S–H gel and cement paste by small-angle neutron scattering, Cem. Concr. Res. 37 (2007) 319–324. doi:10.1016/j.cemconres.2006.09.002.

[78] A.J. Allen, Time-resolved phenomena in cements, clays and porous rocks, J. Appl. Crystallogr. 24 (1991) 624–634. doi:10.1107/S0021889890012237.

[79] S. Brisard, R.S. Chae, I. Bihannic, L. Michot, P. Guttmann, J. Thieme, G. Schneider, P.J.M. Monteiro, P. Levitz, Morphological quantification of hierarchical geomaterials by X-ray nano-CT bridges the gap from nano to micro length scales, Am. Mineral. 97 (2012) 480–483. doi:10.2138/am.2012.3985.

[80] R. Taylor, A. Sakdinawat, S.R. Chae, H.-R. Wenk, P. Levitz, R. Sougrat, P.J.M. Monteiro, Developments in TEM Nanotomography of Calcium Silicate Hydrate, J. Am. Ceram. Soc. 98 (2015) 2307–2312. doi:10.1111/jace.13585.

[81] S. Bae, R. Taylor, D. Shapiro, P. Denes, J. Joseph, R. Celestre, S. Marchesini, H. Padmore, T. Tyliszczak, T. Warwick, D. Kilcoyne, P. Levitz, P.J. M Monteiro, Soft X-ray Ptychographic Imaging and Morphological Quantification of Calcium Silicate Hydrates (C-S-H), J. Am. Ceram. Soc. 98 (2015) 4090–4095. doi:10.1111/jace.13808.

[82] P.W. SCHMIDT, Small-Angle Scattering Studies of Disordered, Porous and Fraetal Systems, J. Appl. Crystallogr. 24 (1991) 414–435.

[83] J.J. Thomas, A.J. Allen, H.M. Jennings, Structural Changes to the Calcium-Silicate-Hydrate Gel Phase of Hydrated Cement with Age, Drying, and Resaturation, J. Am. Ceram. Soc. 91 (2008) 3362–3369. doi:10.1111/j.1551-2916.2008.02636.x.

[84] R.E. Beddoe, K. Lang, Effect of moisture on fractal dimension and specific surface of hardened cement paste by small-angle X-ray scattering, Cem. Concr. Res. 24 (1994) 605–612. doi:10.1016/0008-8846(94)90184-8.

[85] T. Lauridsen, M. Willner, M. Bech, F. Pfeiffer, R. Feidenhans'l, Detection of sub-pixel fractures in X-ray dark-field tomography, Appl. Phys. A. 121 (2015) 1243–1250. doi:10.1007/s00339-015-9496-2.

[86] C. Di Bella, M. Griffa, T.J. Ulrich, P. Lura, Early-age elastic properties of cement-based materials as a function of decreasing moisture content, Cem. Concr. Res. 89 (2016) 87–96. doi:10.1016/j.cemconres.2016.08.001.

[87] C. Di Bella, M. Wyrzykowski, P. Lura, Evaluation of the ultimate drying shrinkage of cement-based mortars with poroelastic models, Mater. Struct. 50 (2017). doi:10.1617/s11527-016-0870-0.

[88] T.C. Hansen, Physical structure of hardened cement paste. A classical approach, Mater. Struct. 19 (1986) 423–436.

[89] S. Diamond, Percolation due to overlapping ITZs in laboratory mortars? A microstructural evaluation, Cem. Concr. Res. 33 (2003) 949–955. doi:10.1016/S0008-8846(02)00996-1.

[90] B. Münch, L. Holzer, Contradicting Geometrical Concepts in Pore Size Analysis Attained with Electron Microscopy and Mercury Intrusion, J. Am. Ceram. Soc. 91 (2008) 4059–4067. doi:10.1111/j.1551-2916.2008.02736.x.

[91] S.K. Lynch, V. Pai, J. Auxier, A.F. Stein, E.E. Bennett, C.K. Kemble, X. Xiao, W.-K. Lee, N.Y. Morgan, H. Harold Wen, Interpretation of dark-field contrast and particle-size selectivity in grating interferometers, Appl. Opt. 50 (2011) 4310–4319.

[92] J. Meiser, M. Amberger, M. Willner, D. Kunka, P. Meyer, F. Koch, a. Hipp, M. Walter, F. Pfeiffer, J. Mohr, Increasing the field of view of x-ray phase contrast imaging using stitched gratings on low absorbent carriers, SPIE Med. Imaging. 01 (2014) 903355. doi:10.1117/12.2043479.

[93] M. Willner, M. Bech, J. Herzen, I. Zanette, D. Hahn, J. Kenntner, J. Mohr, A. Rack, T. Weitkamp, F. Pfeiffer, Quantitative X-ray phase-contrast computed tomography at 82 keV., Opt. Express. 21 (2013) 4155–66. doi:10.1364/OE.21.004155.

[94] P. Li, K. Zhang, Y. Bao, Y. Ren, Z. Ju, Y. Wang, Q. He, Z. Zhu, W. Huang, Q. Yuan, P. Zhu, Angular signal radiography, Opt. Express. 24 (2016) 5829. doi:10.1364/OE.24.005829.

[95] M. Kagias, S. Cartier, Z. Wang, A. Bergamaschi, R. Dinapoli, A. Mozzanica, B. Schmitt, M. Stampanoni, Single shot x-ray phase contrast imaging using a direct conversion microstrip detector with single photon sensitivity, Appl. Phys. Lett. 108 (2016) 234102. doi:10.1063/1.4948584.

[96] M. Kagias, Z. Wang, P. Villanueva-Perez, K. Jefimovs, M. Stampanoni, 2D-Omnidirectional Hard-X-Ray Scattering Sensitivity in a Single Shot, Phys. Rev. Lett. 116 (2016). doi:10.1103/PhysRevLett.116.093902.

[97] M. Marschner, M. Willner, G. Potdevin, A. Fehringer, P.B. Noël, F. Pfeiffer, J. Herzen, Helical X-ray phase-contrast computed tomography without phase stepping, Sci. Rep. 6 (2016) 23953. doi:10.1038/srep23953.

[98] M. Marschner, L. Birnbacher, K. Mechlem, W. Noichl, A. Fehringer, M. Willner, K. Scherer, J. Herzen, P.B. Noël, F. Pfeiffer, Two-shot X-ray dark-field imaging, Opt. Express. 24 (2016) 27032. doi:10.1364/OE.24.027032.

[99] Supplementary Materials available at https://polybox.ethz.ch/index.php/s/993BCDEG5ChDdrf.